

EXPERIMENTAL STUDY OF THERMOACOUSTIC IMAGING SYSTEM

By

GUAN XIN

A DISSERTATION PRESENTED TO THE GRADUATE SCHOOL
OF THE UNIVERSITY OF FLORIDA IN PARTIAL FULFILLMENT
OF THE REQUIREMENTS FOR THE DEGREE OF
DOCTOR OF PHILOSOPHY

UNIVERSITY OF FLORIDA

2012

© 2012 Xin Guan

To my parents and my wife

ACKNOWLEDGMENTS

Thanks to my advisor, Professor Henry Zmuda, for his kind help and excellent guidance for my research work. Without him, I could not have the achievement today. Thanks to Professor Jian Li, for her kind help to assist me in understanding the Robust Capon Beamforming algorithm, which is the major algorithm used and implemented in my thesis. Thanks to Professor Mark Sheplak for his helpful advices on acoustic measurement and theoretical analysis for thermoacoustic imaging. Thanks to Professor Louis Cattafestta for his kind help on data measurement and all the discussions we have had.

TABLE OF CONTENTS

	<u>page</u>
ACKNOWLEDGMENTS.....	4
LIST OF TABLES.....	7
LIST OF FIGURES.....	8
ABSTRACT	11
CHAPTER	
1 INTRODUCTION	13
1.1 Thermoacoustic Imaging.....	13
1.2 Research Background	16
1.2.1 Research in Professor Lihong Wang’s Group	16
1.2.2 Research in Professor Kruger’s Group.....	22
1.3 Thesis Organization.....	25
2 THERMOACOUSTIC SIGNAL GENERATION	28
2.1 CW Microwave Stimulation	28
2.1.1 Diebold Solution	28
2.1.2 Resonant Thermoacoustic Signal Generation	32
2.1.3 RF Amplitude Modulation	35
2.1.4 CW Stimulation Experiment.....	37
2.2 Pulsed Microwave Excitation	40
3 IMAGING ALGORITHM AND FPGA IMPLEMENTATION.....	43
3.1 Digital Beamforming.....	43
3.2 Robust Capon Beamforming Algorithm.....	46
3.2.1 Standard RCB For Narrowband Signal.....	46
3.2.1.1 Capon Beamforming	46
3.2.1.2 Robust Capon Beamforming.....	48
3.2.1.3 Numerical simulation.....	49
3.2.2 Time Delayed RCB for Wideband Signal.....	53
3.2.3 Computational Complexity for Different Algorithm Implementation	55
3.3 FPGA Implementation of RCB	58
3.3.1 Implementation of Standard RCB	60
3.3.1.1 System block diagram.....	60
3.3.1.2 Complex Multiply and Accumulate Unit.....	61
3.3.1.3 Extended Cyclic Jacobi Method	62
3.3.1.4 Lagrange Multiplier Solver	65
3.3.1.5 Adaptive Weight Calculation	66

3.3.1.6 FPGA implementation	67
3.3.2 Implementation of Wideband RCB	68
3.3.2.1 Cyclic Jacobi Method for Eigendecomposition	69
3.3.2.2 FPGA implementation of wideband RCB	72
4 EXPERIMENTAL RESULTS OF THERMOACOUSTIC IMAGING SYSTEM.....	73
4.1 Experimental Step-up of TAI System	73
4.1.1 Introduction.....	73
4.1.1.1 High Power Subsystem.....	74
4.1.1.2 Transducer array subsystem.....	77
4.1.1.3 DAQ subsystem	79
4.2 Thermoacoustic Signal Generation Experiment.....	83
4.3 Thermoacoustic Imaging Experiment.....	87
4.4 Imaging Results	90
5 CONCLUSION.....	94
5.1 Contribution	94
5.2 Future Work.....	95
LIST OF REFERENCES	97
BIOGRAPHICAL SKETCH.....	101

LIST OF TABLES

<u>Table</u>		<u>page</u>
1-1	Typical Dielectric Properties of Breast Tissue	15
2-1	Peak Power Levels for different experiment setup	39
3-1	Resource Utilization for RCB Implementation	67
3-2	Resource Utilization for Wideband RCB Implementation	72

LIST OF FIGURES

<u>Figure</u>		<u>page</u>
1-1	Schematic of Thermoelastic effects	15
1-2	Schematic of Experimental Setup for Professor L. V. Wang's Group	16
1-3	Schematic of the circular measurement configuration	20
1-4	Schematic of the new combined imaging system	22
1-5	Schematic of Experimental Setup for Professor Kruger's Group	22
1-6	Schematic of New Experimental Setup for Professor Kruger's Group	25
2-1	Amplitude frequency response with density ratio = 1	33
2-2	Frequency spectrum with density ratio scanned from 1 to 5.....	34
2-3	Frequency spectrum with density ratio scanned from 1 to 0.6.....	34
2-4	Experiment Schematic for CW Excitation	37
2-5	Output Signal on Spectrum Analyzer with 150 kHz Input Signal	38
2-6	Numerical simulation for pulsed microwave stimulation	42
3-1	Adaptive Antenna Array.....	43
3-2	Beamforming Network.....	45
3-3	System Diagram of Adaptive Beamformer	45
3-4	Signal Comparison	51
3-5	SCB Filtered Signal	51
3-6	RCB Filtered Signal	52
3-7	Beam Pattern Plot	52
3-8	Power Estimates Plot	53
3-9	Illustration of time delayed RCB	54
3-10	Schematic for Computational Complexity Analysis for Matrix Multiplication	56
3-11	Run-time Performance Comparison	57

3-12	System Block Diagram	60
3-13	Datapath of Complex MAC Module	61
3-14	Datapath for Eigenvalue Decomposition Module.....	63
3-15	Datapath for CORDIC Processor.....	64
3-16	Datapath for Diagonal Processing Element.....	65
3-17	Datapath of Lagrange Multiplier Solver	65
3-18	Datapath for Eigenvalue Decomposition Module.....	70
3-19	Datapath for CORDIC Processor.....	71
3-20	Datapath for Diagonal Processing Element.....	71
3-21	Datapath of Off-Diagonal Processing Element	71
4-1	TAI System Block Diagram.....	73
4-2	High Power Subsystem	74
4-3	Control Panel of Pulse Generator.....	75
4-4	Summary of Operational Conditions.....	76
4-5	Transducer	77
4-6	Motor and Transducer System	78
4-7	Scanning Schematic.....	79
4-8	DAQ Subsystem Schematic	80
4-9	Pulser/Receiver Operating Parameters	80
4-10	Configuration for NI 5122 Digitizer.....	81
4-11	Trigger Setting for NI 5122 Digitizer	82
4-12	Control Panel.....	83
4-13	Tank without phantom (right), Tank with phantom (left).....	84
4-14	Relative Positions between Transducer and Phantom	84
4-15	Thermoacoustic Signal in the First Experiment	85

4-16	Zoom-in View of the Thermoacoustic Signal	86
4-17	Thermoacoustic Signal in the Second Experiment	87
4-18	Thermoacoustic Signal in the Third Experiment	87
4-19	New Experimental Tank	88
4-20	Schematic of the phantom.....	89
4-21	Thermoacoustic signals at 0, 120, 240 degree	89
4-22	Imaging Result with 4mm 15% salt phantom using RCB.....	90
4-23	Imaging Result with 4mm 15% salt phantom using SCB.....	90
4-24	Imaging Result with 4mm 15% salt phantom using DAS.....	91
4-25	Imaging Result with 2mm phantom using RCB	91
4-26	Imaging Result with 4mm phantom using RCB	92
4-27	Imaging Result with 6mm phantom using RCB	92

Abstract of Dissertation Presented to the Graduate School
of the University of Florida in Partial Fulfillment of the
Requirements for the Degree of Doctor of Philosophy

EXPERIMENTAL STUDY OF THERMOACOUSTIC IMAGING SYSTEM

By

Xin Guan

May 2012

Chair: Henry Zmuda
Major: Electrical Engineering

Thermoacoustic Imaging is a relatively new medical imaging modality, which combines the benefits of pure microwave imaging and conventional ultrasound imaging, achieving both their high image contrast and high spatial resolution respectively. In operation, the soft tissues in the imaging area are exposed to microwave pulses with a high peak power. Upon irradiation, the tissues will absorb the electromagnetic energy, expand in volume and generate a thermoacoustic signal propagating in all directions. A transducer system picks up the generated thermoacoustic signal, which is then amplified, digitized, and transferred to the computer. An image reconstruction program running in the computer solves an inverse problem to obtain the image of the microwave absorption distribution inside the tissue. Cancerous tissue has a relatively strong electromagnetic absorption due to its higher water content [1], and distinguishes itself from other tissues in the image.

An experimental study of the thermoacoustic imaging system is performed in this thesis, which includes building the prototype system, conducting the initial experiments for generating thermoacoustic signals, and obtaining images of different phantoms with this system. At the beginning, CW (Continuous Wave) microwave stimulation was

employed to find the resonance of the phantom, and finally failed for various reasons. Then pulsed microwave radiation was used, and successfully generated the thermoacoustic signal. A single transducer, coupled with a motor system, was used to simulate a multiple transducer array for data acquisition. Based on the time-delayed Robust Capon Beamforming (RCB) algorithm, several images were acquired from different phantoms.

A Field Programmable Gate Arrays (FPGA) device was used to investigate a hardware implementation of the RCB algorithm. Two implementations were achieved, with one realizing the narrowband RCB used in smart antenna systems and another realizing the wideband RCB used in medical imaging. The possibility of making the thermoacoustic imaging system run in real-time is studied in this work.

CHAPTER 1 INTRODUCTION

1.1 Thermoacoustic Imaging

Breast cancer is considered as the most common type of non-skin cancer in women, and the fifth most usual cause of cancer death worldwide among others. The successful treatment of breast cancer greatly depends on the early detection of the malignant tissue. The current primary screening method for breast cancer is X-ray mammography. X-ray is a kind of ionizing radiation, and could be dangerous for human body in frequent usage. During the diagnosis, the patients need to compress their breasts and suffer a lot of pain. In addition, the dense glandular tissue, connective tissue, and the region near chest wall are difficult to image due to their high density [2]. Ultrasound imaging is commonly used as a complementary method to mammography for breast cancer diagnosis. However the poor soft tissue contrast between benign and malignant tumor in breast limits the application of ultrasound imaging in breast cancer diagnosis [2]. Magnetic Resonance Imaging (MRI), which is also used as a complementary imaging technology for breast imaging, could deliver improved tissue contrast. Although the sensitivity of MRI in detecting malignant tissue has been excellent, the most expensive cost of MRI imaging among all other breast imaging modalities hinders the adoption of MRI as a routine screening method for breast cancer [2]. Recently, thermoacoustic imaging has gained a lot of attention as a promising breast cancer screening method. Firstly microwave radiation is non-ionizing and much healthier for the human body than other ionizing radiation, such as X-ray. Secondly, thermoacoustic imaging can deliver the high soft tissue contrast together with high

spatial resolution. In addition, thermoacoustic imaging system is more cost-effective than MRI.

Thermoacoustic imaging is a relatively new imaging modality [3], which irradiates the soft tissue by electromagnetic radiation, such as optical or microwave radiation, records the ultra-sound signal generated by soft tissue, and obtains the image about distribution of electromagnetic absorption inside the soft tissue through various image reconstruction algorithms. The imaging technology using optical radiation is usually called photoacoustic imaging to show differences from microwave induced thermoacoustic imaging.

Conventional microwave imaging depicts the distribution of dielectric property inside soft tissue by impinging microwave beam onto the target and measuring the back-scattered microwave signal. Cancerous tissue has higher permittivity and conductivity (5 to 10 times) than normal tissue due to higher water content in malignant cells as seen in Table 1-1 [4], and generates larger scattered signal which could be exploited to figure out tumor locations. Microwave imaging has better image contrast than ultrasound imaging, but poor resolution because of long wavelength of microwave. On the other side, ultrasound imaging is able to achieve the resolution in millimeter range because of the short wavelength, but has lower image contrast due to the small difference in acoustic property between tumor and normal tissue. Thermoacoustic imaging combines the benefits of both microwave imaging and ultrasound imaging, and therefore has high image contrast due to the large difference in conductivity between tumor and normal tissue, together with high spatial resolution due to the short wavelength of thermoacoustic signal [5].

Table 1-1. Typical Dielectric Properties of Breast Tissue (Source :B. Guo, "Microwave Techniques for Breast Cancer Detection and Treatment," *PhD Thesis*, University of Florida, Gainesville, FL, 2007.)

TISSUES	DIELECTRIC PROPERTIES	
	PERMITTIVITY	CONDUCTIVITY
IMMERSION LIQUID	9	0
CHEST WALL	50	7
SKIN	36	4
FATTY BREAST TISSUE	9	0.4
NIPPLE	45	5
GLANDULAR TISSUE	11-15	0.4-0.5
TUMOR	50	4

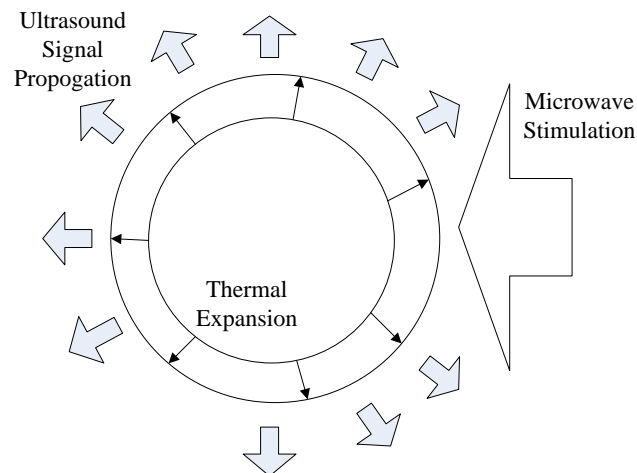


Figure 1-1. Schematic of Thermoelastic effects

In microwave induced thermoacoustic imaging system, pulsed microwave radiation is used to heat the tissue in short duration. After being heated, the tumor expands and generates the acoustic pressure wave as illustrated in Figure 1-1. The acoustic signal is picked up by the ultrasonic transducer or transducer array surrounding the imaging area. After amplification and filtering, the signal is digitized by Analog to Digital (AD) circuitry and processed by image reconstruction algorithm to obtain the

image of conductivity distribution inside the tissue. The peak power of the microwave pulse should be high enough to generate thermoacoustic signal with sufficient signal-to-noise-ratio (SNR) in order to be observable. The recorded signal from AD card is usually averaged multiple times to reduce noise level and increase SNR.

1.2 Research Background

The earliest research about thermoacoustic imaging was published in 1981 by Theodore Bowen [6]. In his paper, issues about thermoacoustic signal generation and detection were investigated, and the possibility of imaging tissue characteristics by thermoacoustic signal was confirmed. James C. Lin published another paper in 1988 [7], in which he discussed some system design issues for thermoacoustic imaging, such as signal detection, signal conditioning and data conversion techniques.

1.2.1 Research in Professor Lihong Wang's Group

In the first paper published in 1999 [8], the experimental setup and initial results were illustrated in details. The schematic is as below.

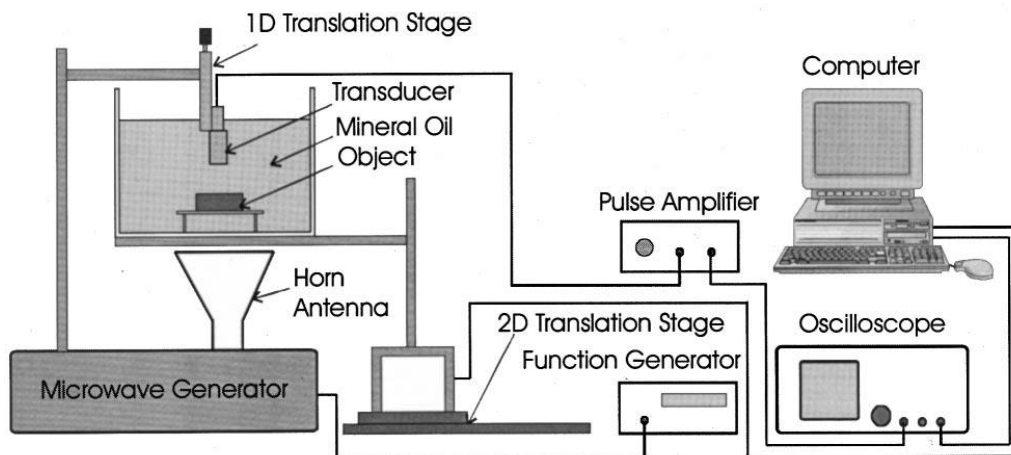


Figure 1-2. Schematic of Experimental Setup for Professor L. V. Wang's Group (Source: L. V. Wang, X. Zhao, H. Sun and G. Ku, "Microwave-induced acoustic imaging of biological tissues," *Review Of Scientific Instruments*, vol. 70, no. 9, pp. 3744-3748, Sep 1999)

In this first experimental setup, they used a 9 GHz microwave source with 10 kW peak power. The thermoacoustic signal was clearly recorded with different power levels and different phantoms used in experiments. Two focused transducers were utilized to receive acoustic signal, with one centered at 1 MHz, bandwidth 0.65 MHz and focal length 2.5 cm at 1 MHz and the other centered at 3.5 MHz, bandwidth 2.5 MHz and focal length 1.8 cm at 3.5 MHz. In this paper, the initial image was acquired for a phantom. The time-resolved thermoacoustic signal recorded by transducer was directly converted to the one-dimensional depth-resolved image. As a result, no image reconstruction algorithm was involved for imaging. In the following papers published in 2000 [1][9], the microwave frequency was changed to 3 GHz because of the less attenuation in soft tissue. As a result, the image obtained is much better than the original image acquired from 9 GHz microwave source. As same as the initial experiment, two focused transducers with different center frequency and bandwidth were utilized to receive thermoacoustic signal. In the first case, the transducer with center frequency 1 MHz and bandwidth 0.6 MHz was deployed for reception. The axial resolution was estimated to be 3.3 mm which coincide with measurement result [1]. In the second case, the transducer with center frequency 3.5 MHz and bandwidth 2.5 MHz was utilized to receive acoustic signal, and the axial resolution was estimated to be 1.4 mm which is also close to experimental result [1]. In experiments, the axial resolution is primarily determined by the pulse width of microwave source and frequency spectrum of the transducer. Shorter microwave pulse and wide-band transducer should result in better axial resolution. The lateral resolution is primarily determined by numerical aperture of the transducer, which is a measure of the capability for transducer to collect ultrasonic

signal and expose the details of sound source at fixed distance. In experiments, the lateral resolution was estimated to 2.1 mm which matches well with measurement result [1].

In paper [10] published in 2001, advanced signal processing technique was used to improve axial resolution and lateral resolution in the original image. The axial resolution is determined by the frequency band of the acoustic signal, while based on analysis about numerical aperture of transducer, the lateral resolution is inversely proportional to the frequency component of the acoustic signal [10]. If we simply use a band-pass filter to get rid of the low frequency noise in acoustic signal, the lateral resolution will be improved, but the axial resolution is sacrificed due to the reduced frequency band of acoustic signal. As a result, a reshaping filter was used for filtering in order to broaden the frequency band and emphasize the high frequency components in acoustic signal. Therefore the axial resolution and lateral resolution were improved at the same time with higher computational complexity.

Until then focused transducer was deployed to detect ultrasound signal and the image was obtained directly from one dimensional time-resolved thermoacoustic signal, meaning that no image reconstruction method was utilized. In paper [11] published in 2001, synthetic aperture method was used for image reconstruction. In experiment, unfocused transducer with center frequency 2.25 MHz was used. Unfocused transducer is able to produce unfocused ultrasound beam in near-field region, and also receive ultrasound signals from all directions with a receiving directivity pattern. Therefore it can be used to record ultrasound signals generated by different parts of phantom and propagating at different directions. The simple and robust synthetic aperture method

(Delay and Sum) was used to reconstruct the image accordingly. In planar measurement configuration with focused transducer, boundaries nearly perpendicular to the acoustic axis of transducer can be imaged clearly, because large part of the thermoacoustic signal generated propagates along the acoustic axis of transducer and is received by transducer. On the other hand, boundaries paralleling to the acoustic axis cannot be imaged, because most of thermoacoustic signal generated propagates perpendicular to the acoustic axis and cannot be received by transducer. This problem was solved by usage of unfocused transducer and synthetic aperture method for image reconstruction. Synthetic aperture method could perform even better in circular or spherical measurement configuration. In paper [12] published in 2001, focused transducer was used in multi-sector scanning to scan the illuminated sample at all directions on a circular trajectory. The image reconstruction method was still the direct method as before and the image was also successfully acquired.

In paper [13] and paper [14] published in 2002, another image reconstruction algorithm, filtered back-projection algorithm, was proposed and used to obtain the image. Filtered back-projection algorithm is the algorithm which tries to reconstruct the original image from projection data obtained from different directions. It's widely used in computed tomography technology. In thermoacoustic imaging research, this algorithm is usually consulted for image reconstruction. At first, the detailed analytical derivation was illustrated [13], which leads to an approximated solution under two assumptions. The first assumption is that the detection radius is usually much larger than wavelength of thermoacoustic signal, and the second assumption states that low frequency component of thermoacoustic signal does not significantly contribute to spatial

resolution [13]. As a result, the modified filtered back-projection algorithm was used as image reconstruction method to depict electromagnetic absorption distribution inside phantom in [14]. The experiment was performed in circular measurement configuration, and unfocused transducer with center frequency 2.25 MHz was deployed to receive thermoacoustic signal. The schematic is showed in Figure 1-3. Microwave pulse was used to illuminate the tissue. In image reconstruction, the filtered back projection algorithm was used. In order to get spatial resolution, point-spread-function (PSF) was calculated. For cutoff frequency of 4 MHz, 2 MHz and 1 MHz, the full width half-maximum (FWHM) of PSF was obtained as 0.4 mm, 0.9 mm and 1.5 mm. In paper [17] published in 2003, time-domain reconstruction algorithm for various measure configuration, including planar, cylindrical and spherical geometry, was unified in one analytical formulation.

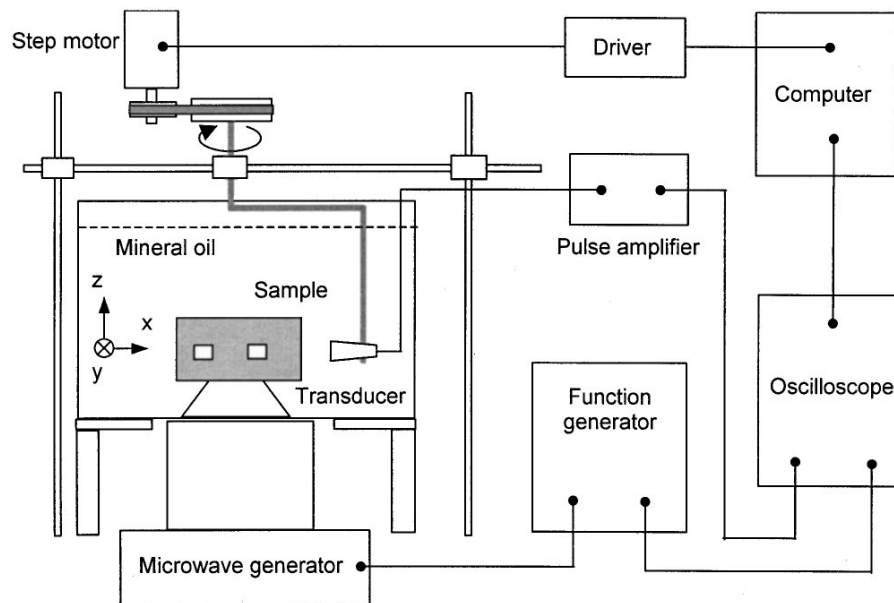


Figure 1-3. Schematic of the circular measurement configuration (Source :M. Xu and L. V. Wang, "Pulsed-microwave-induced thermoacoustic tomography: Filtered backprojection in a circular measurement configuration," *Med. Phys.*, vol. 29, no. 8, pp. 1661-1669, Aug 2002.)

Image reconstruction algorithms mentioned are all based on the assumption that surrounding tissue is acoustically homogeneous, which means that the sound speed and acoustic property should be constant across the entire tissue. However, in real applications, sound speed may vary from 1430 m/s to 1570 m/s around the assumed 1500 m/s [18], and as a result, the phase and amplitude of thermoacoustic signal received at transducer is usually distorted due to heterogeneity of acoustic property across the tissue. In paper [18] published in 2008, a new algorithm, Adaptive and Robust Methods of Reconstruction (ARMOR), was used to perform image reconstruction in thermoacoustic imaging. This algorithm allows amplitude and phase of thermoacoustic signal have some uncertainty, and uses the Robust Capon Beamforming algorithm and peak searching technique to cope with this uncertainty. As a result, image reconstruction became more robust. This ARMOR algorithm was further extended to exploit one more dimension, microwave stimulation frequency, to reduce more noise and interferences in paper [1].

In paper [19] published in 2008, a new device combining thermoacoustic imaging and photo-acoustic imaging was proposed and developed. The schematic of the new device is showed in Figure 1-4. Thermoacoustic imaging can expose the tissue part having high electromagnetic absorption, such as cancerous tissue due to high water content, while photo-acoustic imaging can depict the tissue part showing stronger optical absorption, such as blood vessel. The combination of both medical imaging modalities could enhance early stage cancer detection, and also have several benefits. Firstly, it will reduce the imaging time and is cost effective. Secondly, acquiring two

images on the same setup avoids moving and realigning patient all over again [19].
Imaging results with good quality were achieved on this combined system.

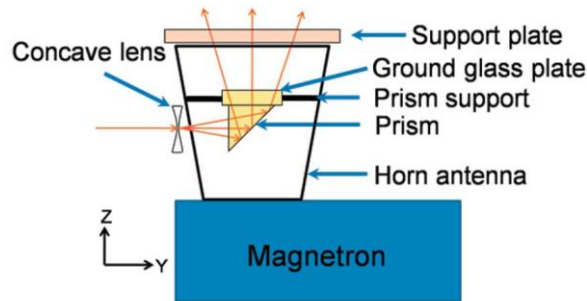


Figure 1-4. Schematic of the new combined imaging system (Source :M. Pramanik, G. Ku and L. V. Wang, etc, “Design and Evaluation of a Novel Breast Cancer Detection System Combining Both Thermoacoustic and Photoacoustic Tomography,” *Med. Phys.*, vol. 35, no. 6, pp. 2218-2223, Jun 2008.)

1.2.2 Research in Professor Kruger’s Group

The first thermoacoustic image was obtained by Dr Robert A. Kruger’s research group. In paper [3] published in 1999, the prototype system was presented with schematic showed below.

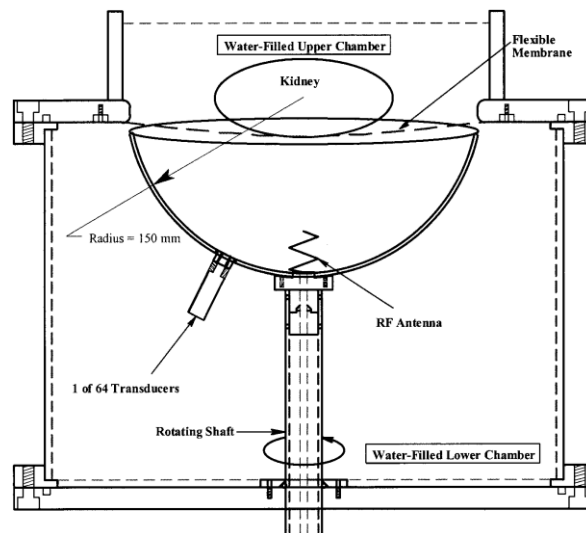


Figure 1-5. Schematic of Experimental Setup for Professor Kruger’s Group (Source :R. A. Kruger, K. K. Kopecky and A. M. Aisen, etc, “Thermoacoustic CT with Radio Waves: A Medical Imaging Paradigm,” *Radiology*, vol. 121, no. 1, pp. 275-278, Apr 1999.)

In this prototype system, 434 MHz microwave pulse with pulse width 0.5 us and peak power 25 kW was used to illuminate the tissue. Repetition rate for microwave pulse was set to 4000 Hz, providing 50 W of average power. Microwave power was fed into the imaging tank by a helical RF antenna, and thermoacoustic signal was picked up by transducer array mounted on the rotational hemisphere bowl, which rotates into many different circular locations to have transducer array receiving acoustic signals in different positions during imaging process. After received by transducer, thermoacoustic signal was amplified and averaged for multiple times in order to increase signal-to-noise -ratio (SNR). The averaged signal was then digitized and transferred to computer. Filtered back-projection algorithm was utilized to perform three-dimensional image reconstruction. Reconstructed image of excised porcine kidney was showed [3].

In paper [20] published in 1999, technical considerations were reported regarding design and implementation of thermoacoustic computed tomography. The approximated Radon transform was used to derive filtered back-projection algorithm for image reconstruction, which lends itself into easy implementation in computer program or special hardware. According to [20], 434 MHz RF radiation was chosen as stimulation frequency based on several reasons. Firstly, electromagnetic absorption for soft tissue is peaked around this frequency range, and 434 MHz is assigned by FCC for medical usage. Secondly, relative SNR of thermoacoustic signal was simulated to peak in the range of 200 – 600MHz. At this low frequency, penetration depth of microwave is adequate for medical imaging application [20]. The positioning of 64 element transducer array was explained in details. Based on the mounting positions of transducer relative to imaging bowl, the rotational movement of the bowl was determined to achieve

maximum coverage for thermoacoustic signal reception. RF heating effects for tissue was also experimented to show that less than 1 degree temperature rise was observed during experiment, which suggests the safety of human being for performing thermoacoustic imaging. The data acquisition scheme and transducer characteristics were also introduced in that paper.

In paper [21] published in 2000, imaging principles of thermoacoustic CT was illustrated in details. Reconstruction methodology based on approximate Radon transform was derived and demonstrated in computer simulation. Spatial resolution was studied extensively using computer simulation. The best spatial resolution near the center axis was showed to be 1.2 mm under 0.5 us microwave pulse stimulation. The limiting factors for spatial resolution were pointed out as the duration of microwave pulse, frequency response of transducer together with associated electronics, and physical size of the face of transducer [21]. Different effects on spatial resolution from different factors were demonstrated by computer simulation.

After that, pilot study of the application of thermoacoustic imaging system on breast cancer detection was conducted, and results were published in the paper in 2001 [22]. Later on, new systems were proposed, built and experimented [23][24]. The schematic is shown below in Figure 1-6. Waveguide array was used to feed microwave pulse into imaging tank in order to make the electromagnetic field distribution more uniform than previous situation. Planar transducer array was used to replace discrete transducer with improved sensitivity, frequency response and immunity to electromagnetic induction (EMI). Another imaging system was described in 2010 paper by Kruger,et. al [25], which combined thermoacoustic imaging, photoacoustic imaging

and ultrasound imaging modalities together. The co-registered image by different imaging technologies was presented in that paper.

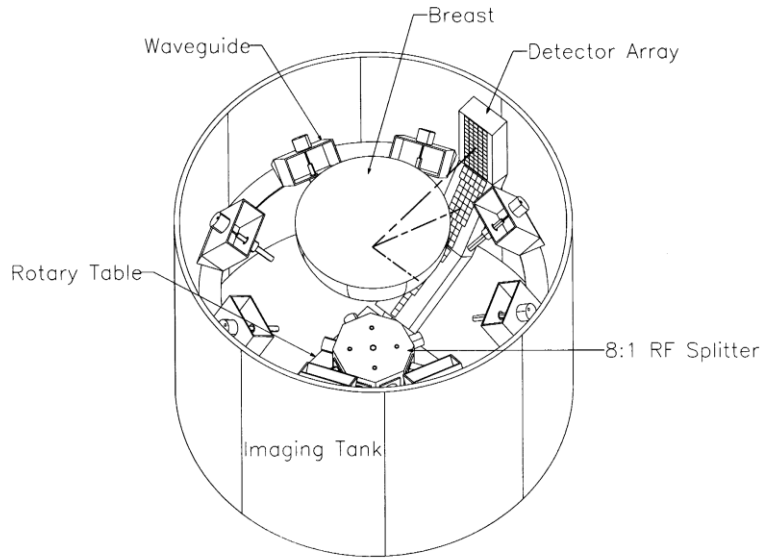


Figure 1-6. Schematic of New Experimental Setup for Professor Kruger's Group (Source :R. A. Kruger, K. Stantz and W. L. Kiser, "Thermoacoustic CT of the Breast," *Medical Imaging 2002: Physics of Medical Imaging*, pp. 521-525, May 2002.)

There are also many other research groups working on this topic. Da Xing's group proposed and developed fast thermoacoustic imaging system with large transducer array and parallel data acquisition system to reduce data collection time, which is described in their paper published in 2006 [26]. They performed research for enhancing thermoacoustic image by microwave contrast agent in [27]. In [28], the feasibility of detecting renal calculi using thermoacoustic imaging technique was investigated.

1.3 Thesis Organization

In Chapter 2, theoretical analysis of thermoacoustic signal generation is presented. Firstly, the analysis for thermoacoustic signal generation under CW microwave stimulation is presented. Diebold solution is showed to depict frequency

response of a spherical phantom upon heating, which points out the possibility of resonance of phantom in time varying heating condition. Amplitude modulation technique for RF signal is then presented, in order to provide baseband time varying heating function. After introducing negative experimental results for thermoacoustic signal generation under CW microwave stimulation, reasons for the discrepancy between theoretical analysis and experimental results are discussed. At last, theoretical analysis for pulsed microwave-induced thermoacoustic signal generation from Professor Lihong Wang's research is quoted to complete the analysis for thermoacoustic signal generation.

In Chapter 3, the major imaging algorithm used in our thermoacoustic imaging application is discussed. First, original narrowband Robust Capon Beamforming algorithm [29] is outlined, together with simulation results. Second, extended wideband Robust Capon Beamforming algorithm used in our medical imaging application is introduced [18]. After discussing software implementation of the algorithm, proposed FPGA implementation of the algorithm is presented. Two implementations are developed respectively for narrowband and wideband Robust Capon Beamformer. The current implementation is still an initial version, which needs to be improved to satisfy the real-time requirements.

In Chapter 4, current experimental setup is introduced as three subsystems, high power subsystem, transducer array subsystem and DAQ subsystem. Experimental results of our thermoacoustic imaging system are presented, including typical thermoacoustic signal waveform and initial imaging results. Different sets of phantom

are experimented, and results are compared. The current imaging functionality and limitations are pointed out in this Chapter.

In Chapter 5, contributions of our thermoacoustic imaging research are identified. In addition, future works are presented.

CHAPTER 2 THERMOACOUSTIC SIGNAL GENERATION

When electromagnetic or optical radiation impinges on soft tissue, energy is absorbed leading to heating effects, and subsequent expansion of the tissue gives rise to acoustic wave which can be picked up by transducer. This is called thermoacoustic or photoacoustic effects, and has been the research topic for a long time in order to utilize this phenomenon for imaging purpose or characterization of different particulate matter. In experiments, usually short pulse of electromagnetic or optical radiation with high enough energy density is used to trigger observable thermoacoustic or photoacoustic signal which is above noise floor.

2.1 CW Microwave Stimulation

2.1.1 Diebold Solution

G. J. Diebold, etc, performed research on photoacoustic effects generated by a spherical droplet in fluid. In their paper published in 1988 [30], the analytical solution of the generated acoustic wave was presented in frequency domain and time domain. Major derivations are listed as follow. If electromagnetic radiation is modulated with baseband frequency ω_m , and the travel time of electromagnetic wave can be neglected, energy absorbed by phantom can be formulated in equation 2.1 as below:

$$H = \alpha I_0 e^{-j\omega_m t} \quad (2-1)$$

where I_0 is the illumination intensity, α is the absorption coefficient of phantom material and H is the amount of energy absorbed per unit volume per unit time. Under thermal confinement condition (the duration of heating pulse should be short enough so that heat conduction to surrounding environment could be neglected), the inhomogeneous wave equation inside the sphere is presented below:

$$\nabla^2 p_s - \frac{1}{c_s^2} \frac{\partial^2 p_s}{\partial t^2} = \frac{-\beta}{C_p} \frac{\partial H}{\partial t} \quad (2-2)$$

where p_s is the pressure wave generated by heating, c_s is the sound speed in phantom, β is thermal expansion coefficient and C_p is specific heat of phantom material.

Substituting equation (2-1) into equation (2-2), we can get the following equation (2-3):

$$\nabla^2 p_s - \frac{1}{c_s^2} \frac{\partial^2 p_s}{\partial t^2} = \frac{j\omega_m \alpha I_0 \beta}{C_p} e^{-j\omega_m t} \quad (2-3)$$

Due to symmetrical condition, we can further assume spherically symmetric solution as $p_s = R(r)e^{-j\omega_m t}$, and plugging into equation (2-3) yields:

$$\frac{\partial^2 R}{\partial r^2} + \frac{2}{r} \frac{\partial R}{\partial r} + k_s^2 R = \frac{j\omega_m \alpha I_0 \beta}{C_p} \quad (2-4)$$

where $k_s = \frac{\omega_m}{c_s}$ is the wave number inside phantom. With particular solution $R_{part} =$

$\frac{j\alpha I_0 \beta c_s^2}{\omega_m C_p}$ and homogeneous solution $R_h = \frac{\sin k_s r}{k_s r}$, the full solution for pressure wave inside

phantom body is listed below,

$$p_s = \frac{j\alpha I_0 \beta c_s^2}{\omega_m C_p} \left(1 + A \frac{\sin k_s r}{k_s r} \right) e^{-j\omega_m t} \quad (2-5)$$

and the full solution for pressure wave outside phantom body is showed as following,

$$p_f = B \frac{e^{j(k_f r - \omega_m t)}}{k_f r} \quad (2-6)$$

where $k_f = \frac{\omega_m}{c_f}$ is the wave number outside phantom, and c_f is sound speed of

surrounding liquid. Terms A , B in the equations above are unknown coefficients which need to be determined by applying boundary condition.

Until now, we have got the analytical expression of pressure wave inside the spherical phantom and outside the phantom. Then pressure and normal velocity are matched at interface. Regarding acceleration, Euler's equation: $\rho \frac{\partial u_r}{\partial t} = -\nabla p$ should be

consulted, where ρ is density, u_r is axial velocity and p is pressure. After setting pressure and normal velocity from inside and outside phantom to be equal at interface, two unknown coefficients A and B can be solved as below:

$$A = \frac{\frac{\rho_s}{\rho_f}(jk_f a - 1)}{\cos k_s a + \left(\frac{\rho_s}{\rho_f} - 1\right) \frac{\sin k_s a}{k_s a} - j \frac{\rho_s k_f}{\rho_f k_s} \sin k_s a} \quad (2-7)$$

$$B = \frac{j\alpha I_0 \beta c_s^2}{\omega_m C_p} \frac{k_f a}{e^{jk_f a}} \left(1 + \frac{\frac{\rho_s}{\rho_f}(jk_f a - 1)}{\cos k_s a + \left(\frac{\rho_s}{\rho_f} - 1\right) \frac{\sin k_s a}{k_s a} - j \frac{\rho_s k_f}{\rho_f k_s} \sin k_s a} \frac{\sin k_s a}{k_s a} \right) \quad (2-8)$$

where ρ_s is the density of phantom material, ρ_f is the density of surrounding liquid, a is radius of the spherical phantom. Substituting equations (2-7) and (2-8) into equations (2-5) and (2-6) yields the pressure wave solution inside and outside phantom as below:

$$p_s = \frac{j\alpha I_0 \beta c_s}{k_s C_p} \left(1 + \frac{\frac{\rho_s}{\rho_f}(1 - jk_f a)}{\left(1 - \frac{\rho_s}{\rho_f}\right) \frac{\sin k_s a}{k_s a} - \cos k_s a + j \frac{\rho_s k_f}{\rho_f k_s} \sin k_s a} \frac{\sin k_s r}{k_s r} \right) e^{-j\omega_m t} \quad (2-9)$$

$$p_f = \frac{j\alpha I_0 \beta c_s a}{k_s C_p} \left(\frac{\frac{\sin k_s a}{k_s a} - \cos k_s a}{\left(1 - \frac{\rho_s}{\rho_f}\right) \frac{\sin k_s a}{k_s a} - \cos k_s a + j \frac{\rho_s k_f}{\rho_f k_s} \sin k_s a} \right) \frac{e^{j(k_f(r-a))}}{r} e^{-j\omega_m t} \quad (2-10)$$

In order to further simplify the expression, we introduce following dimensionless terms:

$$\hat{t} = \frac{c_s}{a} t \quad \text{dimensionless time}$$

$$\hat{t} = \frac{c_s}{a} \left[t - \frac{(r-a)}{c_f} \right] \quad \text{retarded time}$$

$$q = k_s a \quad \text{wave vector}$$

$$\hat{r} = \frac{r}{a} \quad \text{relative distance from sphere center}$$

Plugging in the terms above, inner and outer solution of pressure wave can be formulated as follow:

$$p_s = \frac{j\alpha I_0 \beta c_s a}{C_p q} \left[1 + \frac{\frac{\rho_s}{\rho_f} \left(1 - j \frac{c_s}{c_f} q\right) \left(\frac{\sin q \hat{r}}{q \hat{r}}\right)}{\left(1 - \frac{\rho_s}{\rho_f}\right) \frac{\sin q}{q} - \cos q + j \frac{\rho_s c_s}{\rho_f c_f} \sin q} \right] e^{-jq \hat{t}} \quad (2-11)$$

$$p_f = \frac{j\alpha I_0 \beta c_s a}{C_p \hat{r}} \left[\frac{(\sin q - q \cos q) \frac{1}{q^2}}{\left(1 - \frac{\rho_s}{\rho_f}\right) \frac{\sin q}{q} - \cos q + j \frac{\rho_s c_s}{\rho_f c_f} \sin q} \right] e^{-jq \hat{t}} \quad (2-12)$$

By using time harmonic function for heating, thermoacoustic pressure wave is solved analytically in frequency domain. Impulse response of thermoacoustic process in time domain could be found by performing Inverse Fourier Transform on frequency domain solution. Thermoacoustic pressure wave under radiation with arbitrary temporal profile could be found by convolving impulse response with temporal radiation profile. Detailed derivation is presented in [30].

2.1.1.1 Harmonic Solution in Cylindrical Coordinate System

The frequency domain solution in previous section is achieved in spherical coordinate system while their experiment was conducted for the spherical droplet in a fluid. However our thermoacoustic imaging experiment was performed in cylindrical coordinate system in which the phantom was made into tall cylinder. Therefore we parallel the theoretical analysis above for cylindrical coordinate system to make the derivation complete. After we substituting the heating function in equation (2-1) into the wave equation in (2-2), we end up with the differential equation (2-3). If we assume symmetrical condition and infinite cylindrical source, equation (2-3) could be simplified as:

$$\frac{\partial^2 R}{\partial r^2} + \frac{\partial R}{r \partial r} + k_s^2 R = \frac{j \omega_m \alpha I_0 \beta}{C_p} \quad (2-13)$$

where $k_s = \frac{\omega_m}{c_s}$ is the wave number inside phantom. With particular solution $R_{part} =$

$\frac{j\alpha I_0 \beta c_s^2}{\omega_m c_p}$ and homogeneous solution $R_h = J_0(k_s r)$, the full solution for pressure wave

inside phantom body is listed below,

$$p_s = \frac{j\alpha I_0 \beta c_s^2}{\omega_m c_p} [1 + AJ_0(k_s r)] e^{-j\omega_m t} \quad (2-14)$$

and the full solution for pressure wave outside phantom body is showed as following,

$$p_f = BH_0^{(2)}(k_f r) e^{-j\omega_m t} \quad (2-15)$$

where $k_f = \frac{\omega_m}{c_f}$ is the wave number outside phantom, and c_f is sound speed of

surrounding liquid. Terms A , B in the equations above are unknown coefficients which need to be determined by applying boundary condition. After matching the pressure and acceleration at the boundary, we could solve the unknown coefficients A , B as follow,

$$A = \frac{\rho_s k_f H_1^{(2)}(k_f a)}{\rho_f k_s J_1(k_s a) H_0^{(2)}(k_f a) - \rho_s k_f J_0(k_s a) H_1^{(2)}(k_f a)} \quad (2-16)$$

$$B = \frac{j\alpha \beta I_0 c_s^2}{\omega_m c_p} \left[\frac{\rho_f k_s J_1(k_s a)}{\rho_f k_s J_1(k_s a) H_0^{(2)}(k_f a) - \rho_s k_f J_0(k_s a) H_1^{(2)}(k_f a)} \right] \quad (2-17)$$

Substituting equation (2-17) into equation (2-15), we could find the full solution for pressure wave outside phantom as equation (2-18).

$$p_f = \frac{j\alpha \beta I_0 c_s^2}{\omega_m c_p} \left[\frac{\rho_f k_s J_1(k_s a)}{\rho_f k_s J_1(k_s a) H_0^{(2)}(k_f a) - \rho_s k_f J_0(k_s a) H_1^{(2)}(k_f a)} \right] H_0^{(2)}(k_f r) e^{-j\omega_m t} \quad (2-18)$$

The impulse response of the thermoacoustic process in cylindrical coordinate system could be obtained by applying the Inverse Fourier Transform on the frequency domain solution in equation (2-18).

2.1.2 Resonant Thermoacoustic Signal Generation

According to the analytical solution obtained in previous section, computer simulation has been conducted to study the frequency response of thermoacoustic pressure wave generation process. Different frequency responses are showed in the

plot under varying density ratio, which is obtained through dividing the density of phantom by the density of surrounding liquid. The case when density ratio equals one is used as reference for other situations. Frequency response of the referential situation is illustrated below in Figure 2-1. Multiple peaks appear at a series of resonant frequencies, which give large amplitude amplification, and are relatively broader compared to peaks in larger density ratio cases. In Figure 2-2, a scan of density ratio from 1 to 5 with step size 1 has been performed, and frequency responses are illustrated. Resonant peaks are becoming narrower as density ratio becoming larger, and at the same time resonant frequencies have been shifted a little bit. In Figure 2-3, a scan of density ratio from 0.6 to 1 with step size 0.1 has been performed, and frequency responses are illustrated.

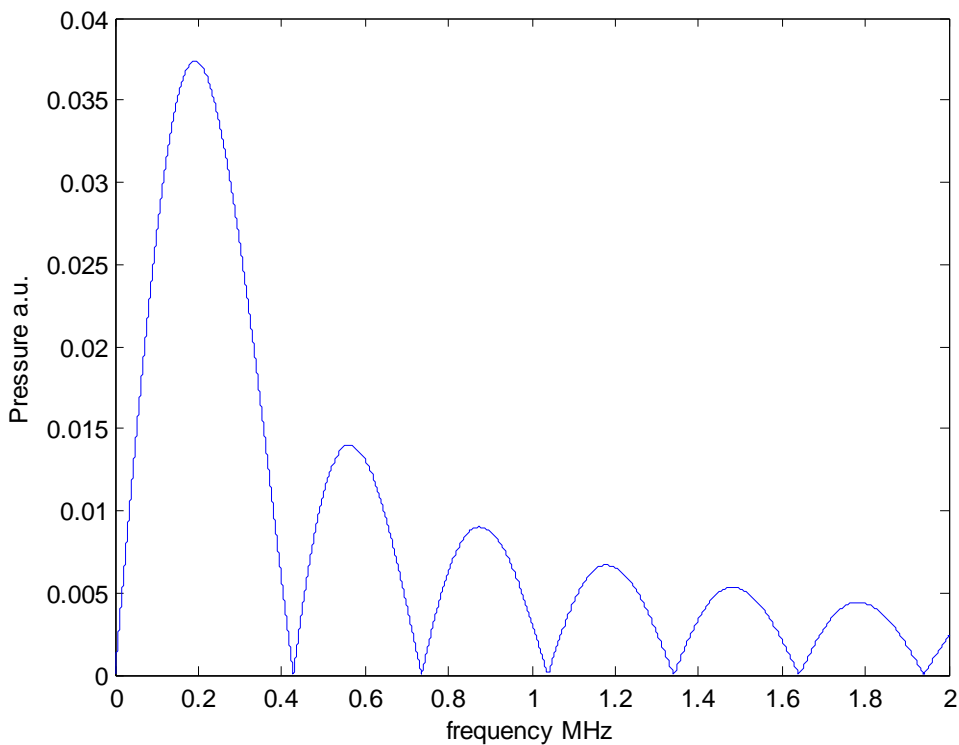


Figure 2-1. Amplitude frequency response with density ratio = 1

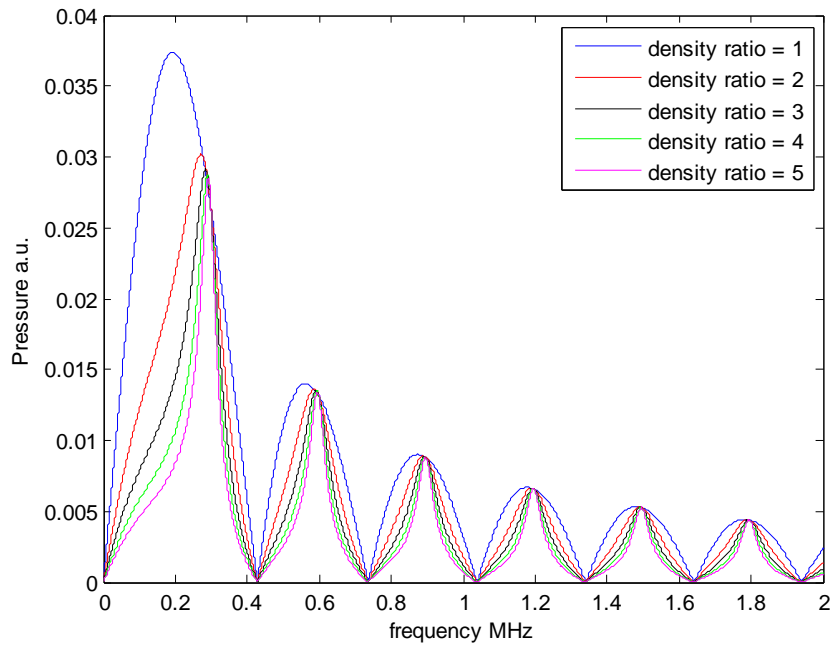


Figure 2-2. Frequency spectrum with density ratio scanned from 1 to 5

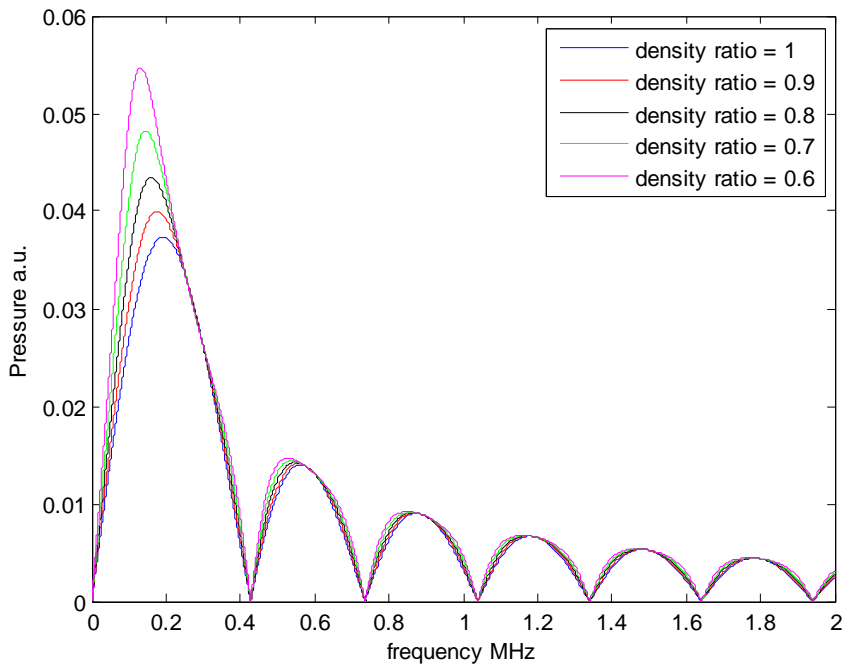


Figure 2-3. Frequency spectrum with density ratio scanned from 1 to 0.6

Based on frequency response presented above, the resonant thermoacoustic imaging idea is developed. Low frequency heating function should be utilized to

stimulate phantom, and the frequency should be swept in certain frequency band to locate the actual resonant frequency. If the resonant frequency was located, lower input power CW stimulation should be applied at this resonant frequency, and larger output signal should be expected due to resonant stimulation. In next section, the technique used to generate low frequency heating function is illustrated, while CW stimulation experiment is described in following section.

2.1.3 RF Amplitude Modulation

In order to get low frequency time-varying heating function, we need to apply amplitude modulation technique on high frequency microwave carrier signal, because baseband RF signal (around 1-2 MHz) will be reflected back from the interface between waveguide and experimental tank due to unmatched electromagnetic impedances on both sides. The relationship between the electric field and the energy absorbed by phantom indicated by equation (2-19) will generate the low frequency heating function, which will serve as the stimulation for phantom. Higher frequency components of heating function should have no effects, because the mechanical expansion and contraction of phantom will not be able to respond at such high frequency. Detailed derivation is illustrated below. SAR (Specific Absorption Rate) can be formulated as equation (2-19).

$$SAR = \frac{\sigma(r)E^2(r,t)}{\rho(r)} \quad (2-19)$$

where $\sigma(r)$ is the conductivity of phantom material, $E(r, t)$ is the intensity of electric field imposed on phantom and $\rho(r)$ is the density of phantom. SAR represents the energy absorbed per unit mass by phantom. Temperature increase can be obtained from thermodynamics principle as follow:

$$\frac{\partial T(r,t)}{\partial t} = \frac{SAR(r,t)}{c_p} = \frac{\sigma(r)E^2(r,t)}{\rho(r)c_p} = C(r)E^2(r,t) \quad (2-20)$$

The temporal formulation of electromagnetic field can be expressed as below assuming uniform heating across phantom body,

$$E(r,t) = A_0[1 + m(t)] \cos \omega_c t \quad (2-21)$$

$$E(r,t) = A_0[1 + A \cos \omega_m t] \cos \omega_c t$$

where $m(t)$ is the low frequency modulation function. Substituting equation (2-21) into equation (2-20) yields:

$$\frac{\partial T(r,t)}{\partial t} = CA_0^2 |(1 + A \cos \omega_m t) \cos \omega_c t|^2$$

in which

$$\begin{aligned} & |(1 + A \cos(\omega_m t)) \cos(\omega_c t)|^2 \quad (2-22) \\ &= \cos^2(\omega_c t) + 2A \cos(\omega_m t) \cos^2(\omega_c t) + A^2 \cos^2(\omega_m t) \cos^2(\omega_c t) \\ &= \frac{1}{2} + \frac{A^2}{4} + A \cos(2\omega_m t) + \left(\frac{1}{2} + \frac{A^2}{4}\right) \cos(2\omega_c t) + \frac{A}{2} [\cos(2\omega_c + \omega_m)t + \cos(2\omega_c - \omega_m)t] \\ &\quad + \frac{A^2}{8} [\cos 2(\omega_c + \omega_m)t + \cos 2(\omega_c - \omega_m)t] \end{aligned}$$

If we suppress carrier signal in modulated signal, meaning that the 1 in the amplitude of electric field is removed, we end up with

$$\frac{\partial T(r,t)}{\partial t} = CA_0^2 |A \cos \omega_m t \cos \omega_c t|^2$$

in which

$$\begin{aligned} & |A \cos(\omega_m t) \cos(\omega_c t)|^2 \quad (2-23) \\ &= A^2 \left[\frac{\cos(\omega_c + \omega_m)t + \cos(\omega_c - \omega_m)t}{2} \right]^2 \\ &= \frac{A^2}{4} + \frac{A^2}{4} \cos(2\omega_m t) + \frac{A^2}{4} \cos(2\omega_c t) + \frac{A^2}{8} [\cos 2(\omega_c + \omega_m)t + \cos 2(\omega_c - \omega_m)t] \end{aligned}$$

From equation (2-22) and (2-23), we can see that there is a low frequency heating component at $2\omega_m$ which can stimulate phantom properly.

2.1.4 CW Stimulation Experiment

Using RF amplitude modulation technique illustrated in previous section, we could generate the low frequency heating function at twice of modulation frequency ω_m . In experiment, it is realized by RF Signal Generator (RFSG) card from National Instruments (NI), which could be programmed by LabVIEW software to generate AM modulated RF signal. Based on the analysis about resonant thermoacoustic imaging, if we apply amplitude modulated RF signal on phantom with an appropriate modulating frequency, we can stand a chance for stimulating phantom at one of its resonant frequencies. Therefore we might be able to leverage this resonant phenomenon to generate thermoacoustic signal with much lower input power. This will save the cost of thermoacoustic imaging system significantly. In experiment, we tried to sweep the modulation frequency in low frequency band with fine resolution and also utilized a RF amplifier to boost the power of RF signal to 100 W for stimulating the spherical phantom. However no thermoacoustic signal was observed but EMI signal, which was believed to be generated by amplifier nonlinearity. The experiment schematic is illustrated in Figure 2-4 below.

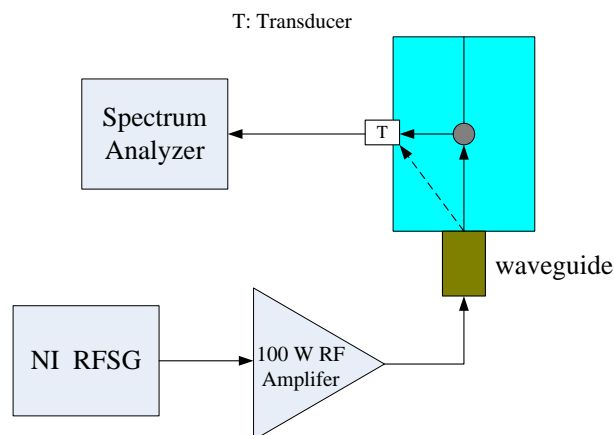


Figure 2-4. Experiment Schematic for CW Excitation

The little sphere inside the tank was a phantom, which was made of distilled water, salt and gelling agent with combinations of different concentration levels, such as 5% salt, 5% gelling agent and distilled water, and this was all wrapped with a piece of rubber. The salt was first dissolved in distilled water. Then gelling agent was added to make the solution become a kind of gel. After that, a finger of rubber glove was cut off and used to wrap the phantom. Transducer was positioned on the tank wall and at the same height with phantom. The transducer used in our experiment was the unfocused immersion transducer from Panametrics NDT, model number V303-SU. Center frequency is around 1 MHz, and 6 dB bandwidth is from 0.687 MHz to 1.25 MHz. RF signal was input from the coaxial to waveguide adaptor at the bottom of tank which primarily produced TE₀₁ mode electromagnetic field, while the output signal from transducer was amplified and displayed on spectrum analyzer. Typical output signal is illustrated in Figure 2-5 below.

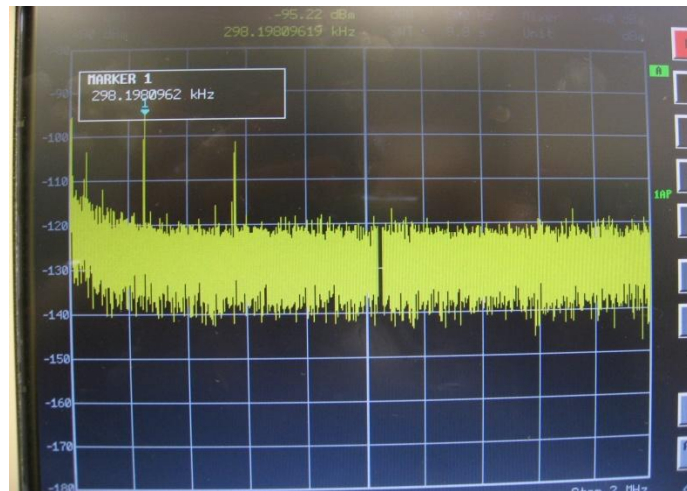


Figure 2-5. Output Signal on Spectrum Analyzer. Photo courtesy of Xin Guan.

In picture above, input signal was set to 150 kHz, and remarkable output signals were located at 300 kHz and 600 kHz, namely at $2\omega_m$ and $4\omega_m$, sometimes even at

higher harmonic frequencies. We swept the modulating frequency from 50 kHz to 2000 kHz with 10 kHz step size, and the $2\omega_m$ and $4\omega_m$ harmonic components kept showing up with no significant changes. The most convincing results should come from comparative study. We did the same frequency sweep with and without phantom in the tank, compared results and couldn't find any remarkable differences. It is believed that this output signal was generated by direct coupling from electromagnetic wave prevailing inside the tank to metal structure inside transducer, and the RF signal on low order harmonic frequencies was generated by nonlinearity of RF amplifier rather than heating effects.

Based on the current experimental results, we can draw the following conclusions about the absence of the thermoacoustic signal. The peak powers of Professor Lihong Wang's experiments, Professor Kruger's experiments, typical Photoacoustic experiments and our CW stimulation experiments are listed and compared in Table 2-1, below. It is showed that our energy density of CW stimulation is far less than all of the other experiments, which makes SNR of thermoacoustic signal too small to be observable. In CW stimulation, heat conduction might also hurt the resonance through damping effects. In addition, the surface tension of the phantom's rubber wrapping may suppress the acoustic vibration of phantom under heating.

Table 2-1. Peak Power Levels for different experiment setup

	PEAK POWER (kW)	ENERGY DENSITY(mJ/cm^3)
Lihong Wang	20	0.45
Kruger	25	0.56
Photoacoustic Imaging	~100	~6
CW Stimulation	< 0.1	<0.0023

Another big concern is related to safety issue. According to IEEE safety standard [31], under a controlled environment, maximum permission exposure (MPE) allows the power density up to 10 mW/cm^2 for human safety. The power density limit is relaxed to 20 mW/cm^2 for partial body exposure. Given dimensions of outlet for our microwave generator ($72 \text{ mm} \times 34 \text{ mm}$), maximum input power should be 0.49 W. Considering reflection due to mismatched impedance at waveguide boundary and microwave attenuation which soft tissue is experiencing, input power could be increased to 10 W or 20 W at most. This power level is far below the threshold power to trigger any observable thermoacoustic signal.

Current thermoacoustic imaging systems are all based on pulsed microwave stimulation, and therefore there is a lack of mature image reconstruction algorithm for CW microwave stimulation. Based on all considerations above, we switched to high peak power pulsed microwave stimulation to construct our thermoacoustic imaging system.

2.2 Pulsed Microwave Excitation

Complete theoretical analysis and numerical simulation for thermoacoustic signal generation is presented in [1], while main ideas are included here for illustration purpose. Under thermal confinement condition, the inhomogeneous wave equation relating deposited microwave energy and generated thermoacoustic pressure wave is presented below.

$$\nabla^2 p_s - \frac{1}{c_s^2} \frac{\partial^2 p_s}{\partial t^2} = \frac{-\beta}{c_p} \frac{\partial H}{\partial t} \quad (2-24)$$

where p_s is the pressure wave generated by heating, c_s is the sound speed in phantom,

β is the thermal expansion coefficient and C_p is specific heat of phantom material per unit mass. The solution for this differential equation can be formulated as below.

$$p_s(\mathbf{r}, t) = \frac{\beta}{4\pi C_p} \iiint \frac{1}{|\mathbf{r} - \mathbf{r}'|} \frac{\partial H(\mathbf{r}', t')}{\partial t'} d\mathbf{r}' \quad (2-25)$$

The position of pressure measuring point is \mathbf{r} , while the source point for thermoacoustic signal is \mathbf{r}' . The integral is calculated inside the sphere centered at \mathbf{r} with radius $c_s t$. t' is calculated as below.

$$t' = t - |\mathbf{r} - \mathbf{r}'|/c_s$$

It is difficult to get an analytic solution for equation (2-25), but for simple geometry, such as a thin slab and under delta heating, pressure wave generated could be formulated as below.

$$p_{slab} = \frac{\beta c_s^2}{2C_p} u(z - c_s t) \quad (2-26)$$

In which $u(z - c_s t)$ is defined as unity between the range $0 \leq (z - c_s t) \leq d$ and zero elsewhere. d is the thickness of slab. If heating function can be expressed temporally by $H(z, t)$, pressure response from this specific heating function can be calculated based on convolution theory as below.

$$p_{total} = \int p_{slab}(z, \tau) H(z, t - \tau) d\tau \quad (2-27)$$

Thermoacoustic pressure signal impinges on transducer, and generates piezoelectric signal observed on oscilloscope. If the impulse response of the transducer can be expressed as $h(t)$, the piezoelectric signal generated can be formulated as below based on convolution theory.

$$s(z, t) = \int p_{total}(z, \tau) h(z, t - \tau) d\tau \quad (2-28)$$

Numerical simulation for thin slab phantom in [1] is listed below for illustration. Figure 2-6 (a) is the thermoacoustic signal from an infinite thin slab under delta heating, and Figure 2-6 (b) is the temporal profile of microwave pulse. Figure 2-6 (c) is the

convolution result of (a) and (b). Figure 2-6 (d) is the impulse response of transducer. Figure 2-6 (e) is the convolution result of (c) and (d).

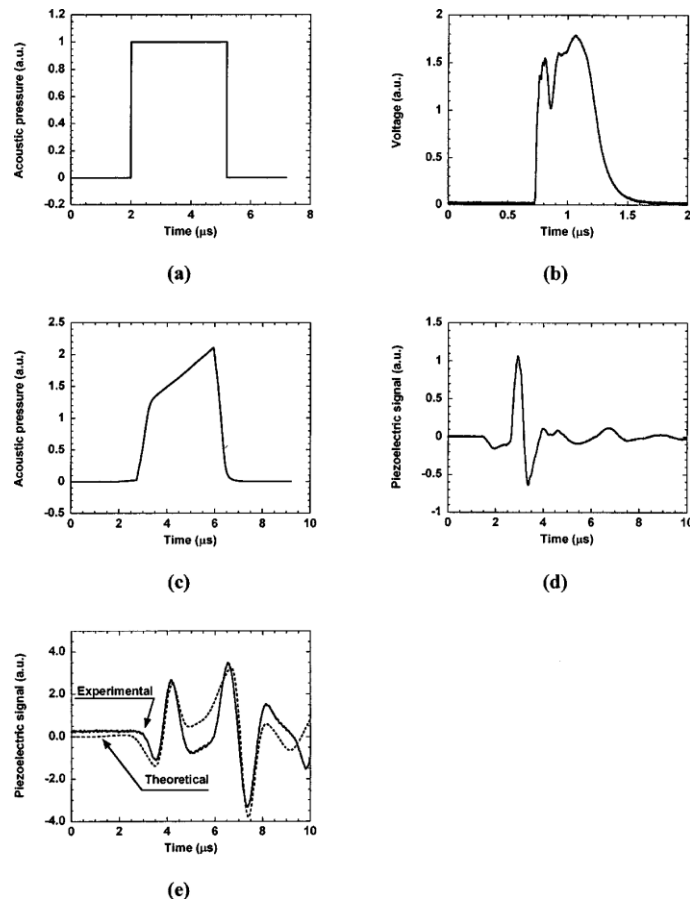


Figure 2-6. Numerical simulation for pulsed microwave stimulation (Source :G. Ku and L. V. Wang, "Scanning thermoacoustic tomography in biological tissue," *Med. Phys.*, vol. 27, no. 5, pp. 1195-1202, May, 2000.)

CHAPTER 3 IMAGING ALGORITHM AND FPGA IMPLEMENTATION

3.1 Digital Beamforming

Beamforming algorithm is a widely used algorithm in array signal processing, with applications ranging from Radar/Sonar systems, wireless communication and medical imaging. Beamformer is basically a spatial filter which operates on output of an array of sensors/antennas in order to enhance the signal-of-interest (SOI) relative to background noise and directional interference [32][33][34]. Conventional beamformer, such as Delay and Sum beamformer, is data independent and robust. However the performance is inferior to adaptive beamformer, which can automatically adapt the spatial filter coefficients to changing signal characteristics as illustrated by Figure 3-1. Adaptive antenna array is showed below, which can adaptively form the beampattern according to moving locations of targeted user and interfering user.

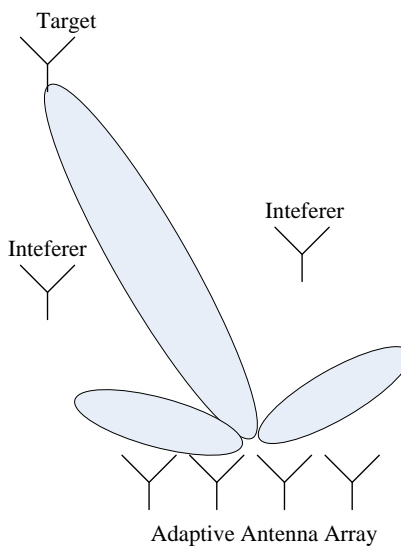


Figure 3-1. Adaptive Antenna Array

Usually beamforming system is working between analog-front-end circuitry and digital baseband processing as illustrated in Figure 3-2. Firstly, the analog signal is

picked up by antenna array in RF application or transducer array in ultrasound application. Then the analog signal is processed by receiver circuitry which performs signal conditioning, such as filtering and amplification. The first stage is commonly a low noise amplifier (LNA) which can amplify the analog signal with as little increase of noise power as possible. Then an analog bandpass filter or lowpass filter is used to wipe out out-of-band noise and interference signals. In RF application, the signal usually needs to be down-converted to intermediate frequency (IF) or to baseband frequency by analog mixer and local oscillator. After these preprocessing, the analog signal is converted to digital signal by ADC (Analog Digital Converter). This series of operation is performed on every channel in antenna array. Digital signals collected from multiple channels are then fed into digital beamforming network, which tries to optimally combine multiple signal streams into one signal stream which has lower noise and interference level. Beamforming output could then be passed down to digital baseband processing stage, such as demodulation in wireless communication application.

Adaptive beamforming network consists of a spatial filter and an adaptive weight update module. The spatial filter actually forms the beam pointing to the desired signal direction and nullifies the strong interference signal using the calculated weight coefficients. The system diagram is showed in Figure 3-3. The adaptive weight calculation module takes channel data information as input, such as desired signal direction, signal covariance matrix or reference signal, calculates adaptive weight coefficients and feeds them into the spatial filter. Weight coefficients are updated as frequent as possible given hardware limitations in order to capture fast-changing signal characteristics.

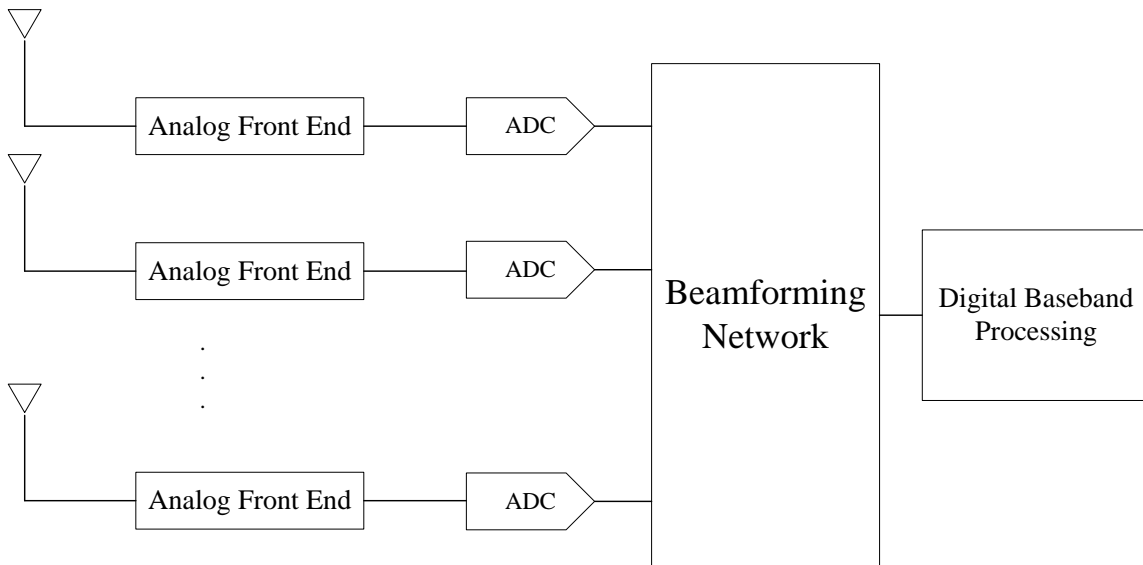


Figure 3-2. Beamforming Network

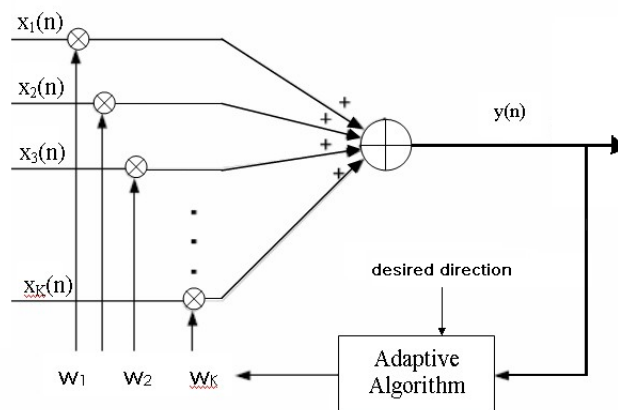


Figure 3-3. System Diagram of Adaptive Beamformer

In our thermoacoustic imaging application, a modified Robust Capon Beamforming algorithm is adopted as imaging algorithm [4][18], because it has superior performance over conventional delay-and-sum beamforming algorithm. The derivation and hardware implementation details of our imaging algorithm will be presented in following sections [52][53].

3.2 Robust Capon Beamforming Algorithm

Adaptive Beamforming is a widely used technology in array signal processing. Its various applications include Radar and Sonar systems, Smart Antenna systems for wireless communications, and medical imaging methods. Capon Beamforming is one of the earliest adaptive beamforming techniques devised. It has the potential to provide significantly better resolution and interference rejection capability compared to conventional delay-and-sum beamformer [32][33][34]. However, it is sensitive to model errors, such as array steering vector errors including array calibration errors and imprecise knowledge of direction of arrival (DOA) of SOI. Many algorithms have been proposed to mitigate this problem, and one of them being the Robust Capon Beamforming (RCB) [29]. This algorithm belongs to diagonal loading class (algorithms which adds a diagonal loading factor in covariance matrix to make it robust for beamforming), and its diagonal loading level can be calculated exactly according to the uncertainty set of array steering vector. Moreover, its computational complexity is comparable to that of Capon beamformer [29][34].

3.2.1 Standard RCB for Narrowband Signal

3.2.1.1 Capon Beamforming

Conventional Beamforming methods such as delay-and-sum beamforming have gained wide use in many applications including medical imaging. It is simple, robust and easy to implement in software or hardware. However its drawbacks include poor resolution and high side lobe levels when compared with other adaptive beamforming approaches. Capon Beamforming is capable of adaptively calculating the required weight vector based on sample covariance matrix obtained from array output data, which passes the SOI in an undistorted manner while placing deep nulls in directions of

interferers [32][33][34], resulting in strong interference suppression. The spatial filtering formulation of Capon Beamforming is summarized below (a detailed derivation of Capon Beamforming can be found in [29]). The data model used here is:

$$\mathbf{y}(n) = \mathbf{a}_0 s_0(n) + \mathbf{e}(n) \quad (3-1)$$

where $\mathbf{y}(n) = [y_1(n), y_2(n), \dots, y_M(n)]^T$ is the received signal vector at array output, with n representing sampling time and M being the number of antenna elements. \mathbf{a}_0 is the true steering vector of SOI, $s_0(n)$ is the waveform of SOI, and the term $\mathbf{e}(n)$ represents interference plus noise. Under the framework of Capon Beamforming, the calculation of weight vector \mathbf{w} can be formulated as the linearly constrained optimization problem given by:

$$\min_{\mathbf{w}} \mathbf{w}^* \mathbf{R} \mathbf{w} \quad \text{subject to } \mathbf{w}^* \mathbf{a}_0 = 1 \quad (3-2)$$

where \mathbf{R} is the theoretical covariance matrix of received signal and $\mathbf{w}^* \mathbf{R} \mathbf{w}$ is the output power of Capon Beamformer. Equation (3-2) illustrates the optimization problem that the total output power is minimized while the SOI is passed undistorted, which indicates that noise and interferences are minimized. The solution to this optimization problem leads to the optimal weight vector of Capon Beamformer:

$$\mathbf{w}_{CB} = \frac{\mathbf{R}^{-1} \mathbf{a}_0}{\mathbf{a}_0^* \mathbf{R}^{-1} \mathbf{a}_0} \quad (3-3)$$

In practical applications, \mathbf{R} is difficult to obtain, and thus is usually replaced by sample covariance matrix $\hat{\mathbf{R}}$ which is calculated from received signal vectors as:

$$\hat{\mathbf{R}} = \frac{1}{N} \sum_{n=1}^N \mathbf{y}(n) \mathbf{y}(n)^* \quad (3-4)$$

where the integer N is the number of snapshots used in beamforming. Also, the true steering vector \mathbf{a}_0 may not be available in practice, and the assumed steering vector $\bar{\mathbf{a}}_0$ is used instead in Equation (3-3). Unfortunately, a slight deviation between the assumed

steering vector and the true steering vector of SOI may cause a significant degradation of performance for Capon Beamformer, because in this case the beamformer treats SOI as an interfering signal. Therefore, numerous algorithms have been derived to improve the robustness of Capon beamforming [29][34].

3.2.1.2 Robust Capon Beamforming

The RCB algorithm implemented in our thermoacoustic imaging project was proposed in [29], which deals with narrow-band complex-valued array signals. The main idea of the algorithm is presented in this section. The algorithm assumes that the true steering vector of SOI can be estimated within an uncertainty set based around the assumed steering vector of SOI. The formulation of RCB is summarized as:

$$\min_{\mathbf{w}} \mathbf{w}^* \hat{\mathbf{R}} \mathbf{w} \text{ subject to } \mathbf{w}^* \mathbf{a} = 1 \quad \|\mathbf{a} - \bar{\mathbf{a}}_0\| \leq \varepsilon \quad (3-5)$$

where ε is a user-defined parameter for the size of the uncertainty set of the true steering vector \mathbf{a} around an assumed steering vector $\bar{\mathbf{a}}_0$. By using a Lagrange multiplier methodology, the constrained optimization problem of RCB above can be solved in four steps:

Step 1. Compute eigendecomposition (EVD) of $\hat{\mathbf{R}}$.

$$\hat{\mathbf{R}} = \mathbf{Q} \mathbf{U} \mathbf{Q}^* \quad (3-6)$$

In equation (3-6), \mathbf{Q} represents eigen-vector matrix, while \mathbf{U} is a diagonal matrix containing eigen-values of $\hat{\mathbf{R}}$ as diagonal elements.

Step 2. An iterative method is used to solve Lagrange multiplier ν from equation (3-7).

$$\sum_{m=1}^M \frac{|z_m|^2}{(1+\nu\lambda_m)^2} = \varepsilon \quad (3-7)$$

where M is the number of antenna elements, z_m is the m^{th} element of vector $\mathbf{z} = \mathbf{Q}^* \bar{\mathbf{a}}_0$,

λ_m is the m^{th} eigen-value of $\hat{\mathbf{R}}$ (all eigen-values are arranged in the increasing order along the diagonal elements of \mathbf{U}), v is the Lagrange multiplier.

Step 3. After obtaining the Lagrange multiplier v , an estimate of the true steering vector for SOI can be calculated from equation (3-8).

$$\hat{\mathbf{a}}_0 = \left(\frac{\hat{\mathbf{R}}^{-1}}{v} + \mathbf{I} \right)^{-1} \bar{\mathbf{a}}_0 \quad (3-8)$$

Step 4. Finally substituting $\hat{\mathbf{a}}_0$ into equation (3-3) yields the optimal weight vector for RCB algorithm:

$$\mathbf{w}_{RCB} = \frac{\hat{\mathbf{R}}^{-1} \hat{\mathbf{a}}_0}{\hat{\mathbf{a}}_0^* \hat{\mathbf{R}}^{-1} \hat{\mathbf{a}}_0} \quad (3-9)$$

A detailed derivation of RCB algorithm can be found in [29].

3.2.1.3 Numerical simulation

Based on the introduced adaptive beamforming algorithm above, numerical simulation is performed in order to compare the performance of standard Capon Beamforming (SCB) and Robust Capon Beamforming (RCB). In the simulation configuration, uniform linear antenna array with 10 antenna elements was assumed. Noise power was set to 0 dB, and the SOI signal power was set to 20 dB at 10 degree (-90 degree to 90 degree), while four strong interferers with 40 dB power were assumed at -75 degree, -60 degree, -10 degree and 25 degree respectively. The assumed DOA of SOI was deliberately set at 11 degree with 1 degree deviation from the true DOA of SOI in order to test the robustness of RCB algorithm.

Antenna elements were positioned at half wavelength separation distance between each other. The waveforms of SOI signal, interferer signals and noise were generated by random sequence generator in order to make them irrelevant to each other. Both the standard Capon Beamforming and Robust Capon Beamforming were

applied to the array data, and tried to pick out the SOI signal. The simulation results are listed in following figures. In Figure 3-4, the blue line is the total received signal at channel 1. The red line is the SOI signal expected to be received at channel 1, while the green line is the interferer signal at channel 1. The black line represents noise which has the same magnitude at all channels. It can be found that the received signal is dominated by the interferer signal because of its higher power level compared to SOI signal. In Figure 3-5, the filtered signal by SCB is compared against SOI waveform. It can be noticed that the SOI is almost filtered out due to the 1 degree deviation between the assumed DOA of SOI and the true DOA of SOI, which vividly demonstrates the lack of robustness of SCB. In Figure 3-6, the filtered signal by RCB is compared against SOI waveform. It can be verified that the SOI is successfully extracted from severely corrupted totally received signal under the 1 degree imprecision of knowledge for DOA of SOI, which confirms the robustness of RCB. In Figure 3-7, the beampatterns of SCB and RCB are plotted together, which tells us why the SCB algorithm filters out the SOI signal while the RCB algorithm maintains the SOI signal. It can be found that at 10 degree where the true SOI comes from, the SCB beampattern forms a deep null killing the SOI signal, because it thought the true SOI signal comes from 11 degree and treats the SOI at 10 degree as an interferer signal, while the RCB beampattern forms a peak which passes through the SOI signal undistorted. In Figure 3-8, power estimates from SCB and RCB are plotted against the true SOI power. It can be found that the power estimate from SCB is far less than the true SOI power, while the power estimate from RCB is around the true SOI power with acceptable error.

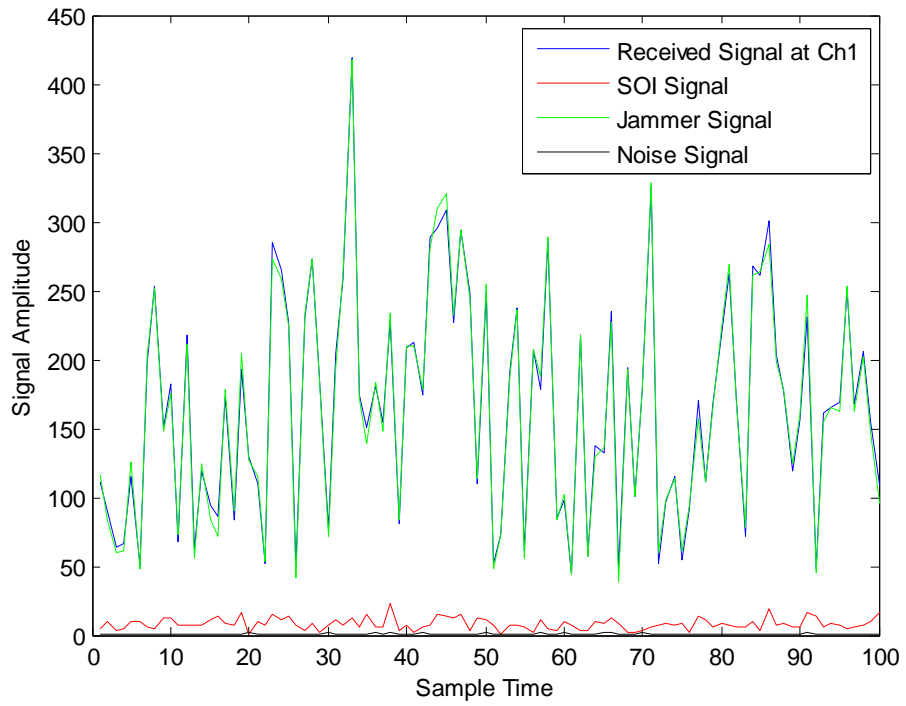


Figure 3-4. Signal Comparison

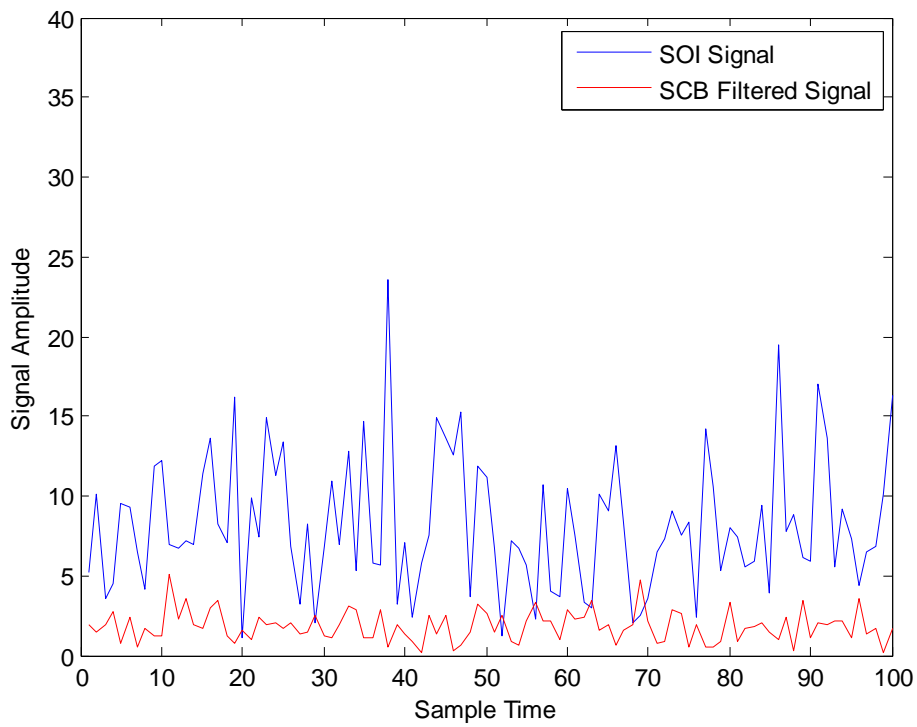


Figure 3-5. SCB Filtered Signal

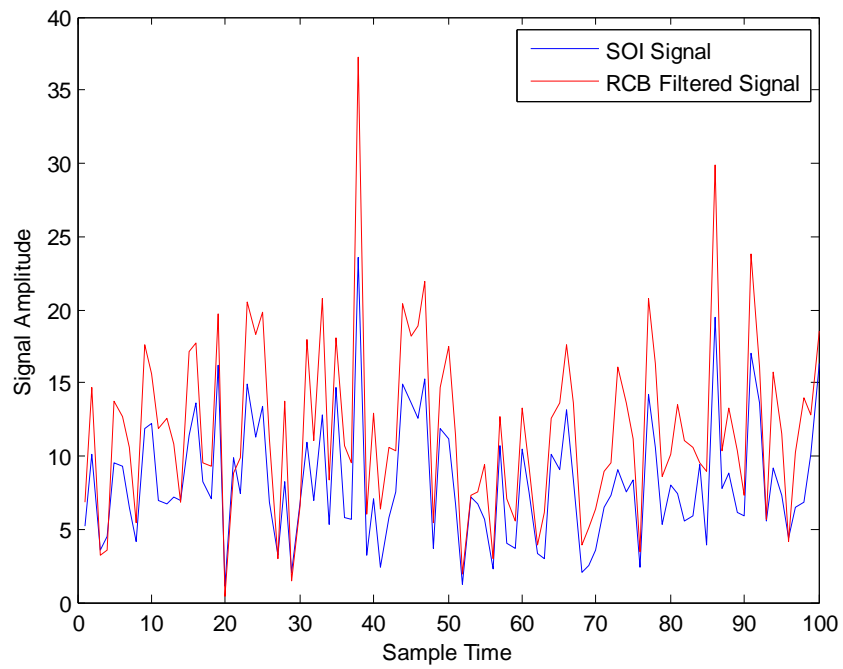


Figure 3-6. RCB Filtered Signal

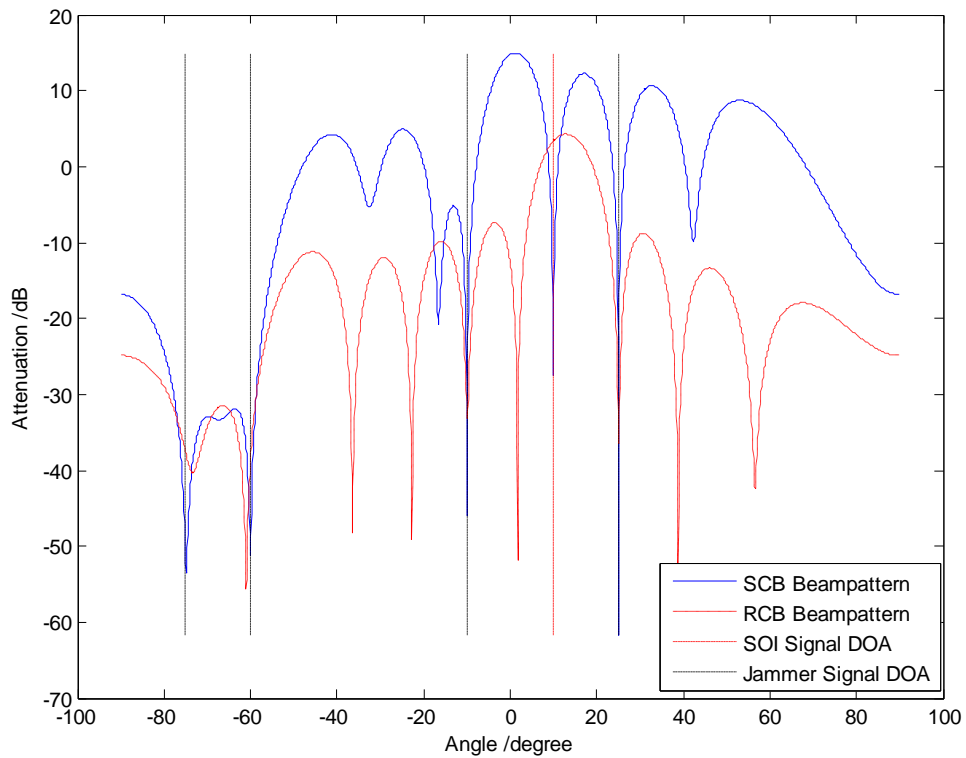


Figure 3-7. Beam Pattern Plot

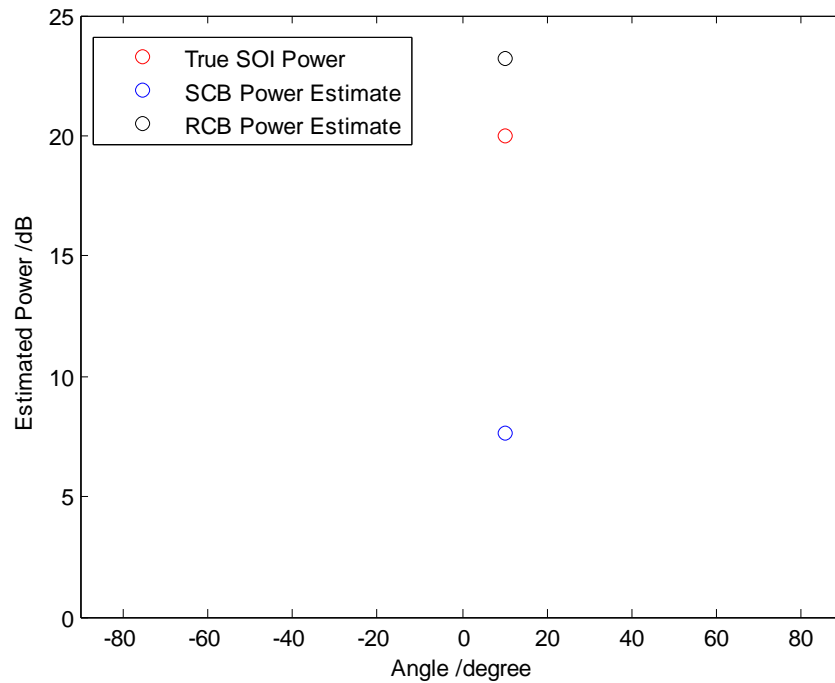


Figure 3-8. Power Estimates Plot

3.2.2 Time Delayed RCB for Wideband Signal

Robust Capon Beamforming algorithm presented above mainly deals with narrowband complex-valued input data. In narrowband situation, the steering vector \mathbf{a} is a complex-valued vector representing the phase and amplitude relationship of received signals among multiple antennas in the array. However, in our thermoacoustic imaging project, the signal picked up by transducer is a broadband (around 1 MHz at baseband) and real signal, which is not able to be processed directly by the original Robust Capon Beamforming algorithm. Another unique issue in our medical imaging application is that the ultrasonic signals received by different transducer channels are experiencing different path losses, and need to be compensated before performing beamforming. Therefore, the original Robust Capon Beamforming algorithm was modified in [4][18], and applied in our thermoacoustic imaging project.

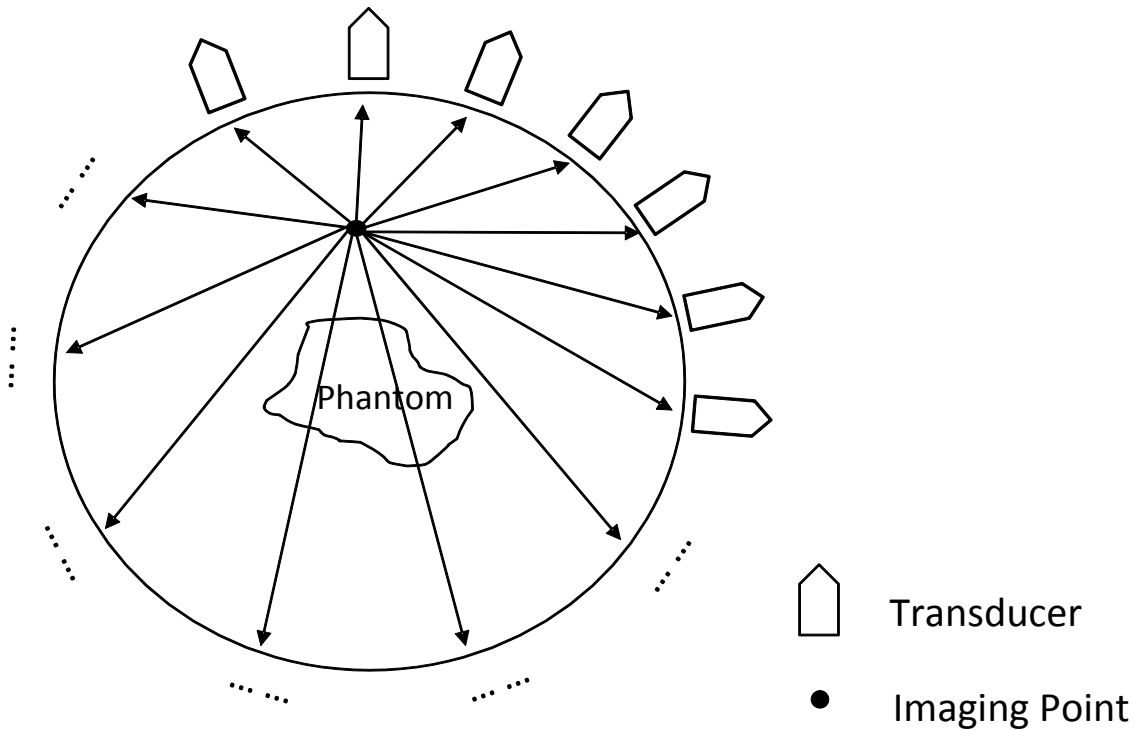


Figure 3-9. Illustration of time delayed RCB

In the modified time-delayed RCB presented in [4][18], acoustic signals picked up by transducers firstly are compensated in amplitude according to different path loss at different channel. Then the compensated signals are aligned in time domain based on different delay on every channel, which is determined by the distance between the imaging point and the transducer. As a result, the steering vector for this specific imaging point has become an all one vector. Subsequent steps follow the standard RCB algorithm with only real-valued data in all computations. After the adaptive weight vector for this imaging point has been calculated, waveforms from multiple transducers are combined using beamforming coefficients just obtained. Energy or peak-to-peak value of the combined waveform is considered to be the image intensity at this specific imaging point. The operation of time-delayed RCB is illustrated in Figure 3-9, in which a typical imaging point is showed. In real operation, the entire imaging area is scanned

point by point with acceptable resolution. In doing so, we can get an image of the intensity of acoustic sources inside the imaging area, which corresponds to the amount of energy absorbed during electromagnetic illumination and directly relates to the conductivity of phantom at that location.

3.2.3 Computational Complexity for Different Algorithm Implementation

Major computational steps for RCB are summarized as matrix multiplication (include calculation of covariance matrix and estimated steering vector, which will be explained in following sections), eigen-value decomposition for symmetric matrix, iterative method for solving Lagrange multiplier and FIR filtering. The most computational intensive tasks are matrix multiplication and eigen-value decomposition for symmetric matrix, which have computational complexity of $O(n^3)$ [29]. The well-known numerical algorithm for eigen-value decomposition is the Cyclic Jacobi Method which is simple, robust and amenable to fixed-point implementation. The computational complexity of Cyclic Jacobi Method is analyzed and presented in [51], which gives also $O(n^3)$ complexity for every sweep in calculation.

In conceptual Microprocessor or DSP processor model, there is only one multiplier and one adder, or more concisely, one MAC operational unit available for computation. Although in modern Microprocessor or DSP processor, there are multiple integer and floating-point functional units available, we can first assume the conceptual model introduced above for simplicity. In our FPGA implementation, we realized linear computational unit array with n dimensions to exploit parallelism in matrix multiplication and eigen-value decomposition in order to speed up computation from the architectural perspective. The schematic for matrix multiplication is listed in Figure 3-10.

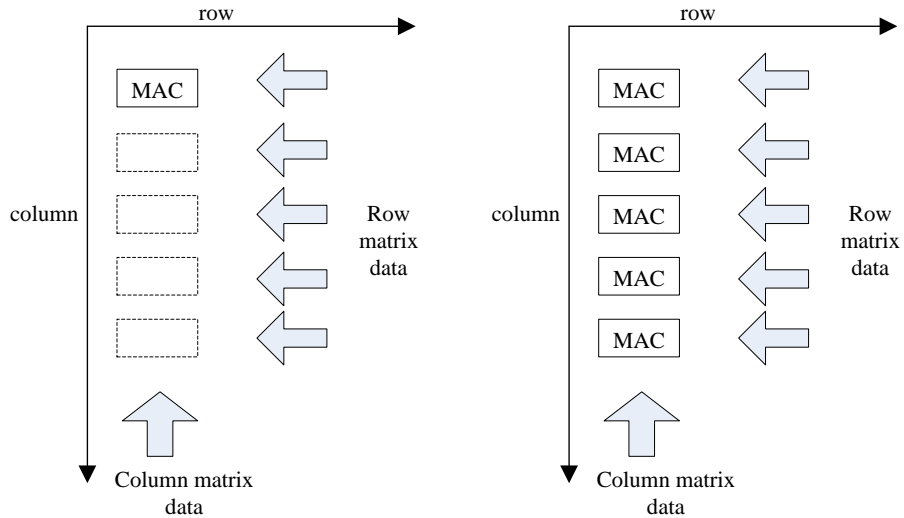


Figure 3-10. Schematic for Computational Complexity Analysis for Matrix Multiplication

The left part of Figure 3-10 represents Microprocessor or DSP processor implementation, which utilize the single MAC unit to perform computations for every single element in result matrix yielding $O(n^3)$ computational complexity. The right part of Figure 3-10 represents FPGA implementation, which utilize the linear MAC unit array to perform computations for every element in single column from result matrix yielding $O(n^2)$ computational complexity.

The same situation occurs in eigen-value decomposition. In Microprocessor or DSP processor implementation, the only computational unit is used to perform computations for every row element in Cyclic Jacobi Method which results in $O(n^3)$ computational complexity. On the other hand, in FPGA implementation, the linear computational unit array is used to perform computations for entire row at the same time, which will speed up computation by n times and yield $O(n^2)$ computational complexity. This will be further illustrated in following sections.

Comparison of run-time performance between software implementation and FPGA implementation are presented as follow. The application is an 8 channel

wideband Robust Capon Beamforming algorithm. Temporary delay and amplitude compensation have been done before testing. As a result, only the computation time is compared. For software implementation, the platform is a Pentium(R) dual-core CPU running at 2GHz in a laptop with 3GB memory, while the platform for FPGA implementation is a Xilinx SX-35 platform device. Computation time scaling with FPGA operating frequency is showed in Figure 3-11. From the chart, we can notice that from the frequency larger than 35 MHz, FPGA implementation should run faster than software implementation. Current running frequency is 80 MHz, which gives FPGA implementation around 2.3 times speedup over software implementation compared with the expected 8 times speedup. It should be noticed that only computation time is considered in comparison while data transfer time from PC to FPGA board is not taken into consideration, which could slow down overall FPGA computation further.

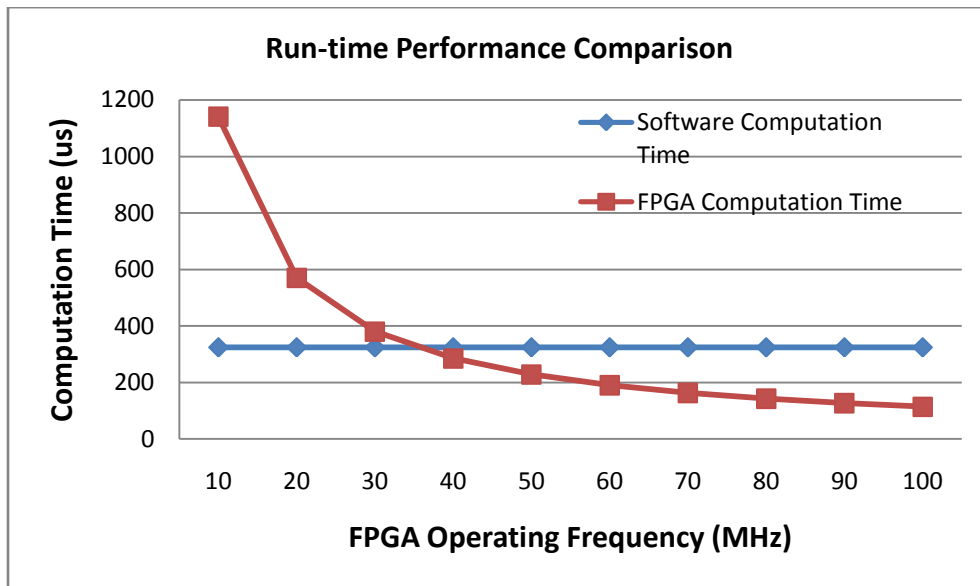


Figure 3-11. Run-time Performance Comparison

3.3 FPGA Implementation of RCB

In previous sections, the principle and computational steps of the RCB algorithm are illustrated in details. This section mainly deals with hardware implementation of the algorithm. For any digital signal processing algorithm, there might be multiple alternative implementations which have different pros and cons. A digital signal processor based implementation is the most flexible and cheap approach to adopt, however it may not provide the best performance. An ASIC (Application Specific Integrated Circuit) specially designed for running beamforming algorithm usually is too expensive to design and fabricate. As long as being manufactured, the chip can't be adapted to algorithmic changes any more. A FPGA (Field Programmable Gate Arrays) provides a good platform for implementing digital signal processing algorithm due to its high processing power and great flexibility when compared with its DSP processor and ASIC counterparts. It is also an ideal platform for algorithm design and verification. Therefore, in our thermoacoustic imaging project, FPGA based hardware implementation of RCB algorithm is investigated and realized on Xilinx Virtex4 SX35 platform.

As illustrated in previous section, compared with Microprocessor or DSP processor implementation, FPGA implementation can exploit parallelism in computation more extensively by utilizing the linear array of computational unit to get a n -fold speed up (n is the dimension of matrix). In reality, this speed-up can be compromised by two factors. First, modern Microprocessor or DSP processor also have multiple computational units such as in Superscalar architecture, but the architecture of computational unit pool is for general purpose usage, which can not be specialized for any specific application. Second, the operating frequency for Microprocessor or DSP processor is much higher than FPGA implementation. As a result, FPGA

implementation may not be faster than Microprocessor or DSP processor implementation in absolute time. However, the research and development of FPGA implementation for RCB is still meaningful in that FPGA implementation of RCB could work as the hardware accelerator, which could save Microprocessor or DSP processor from computational intensive task and let them focus on other essential jobs, such as running Operating System, controlling display. FPGA implementation could also work as the verification platform for ASIC module implementation, which might be included in SOC design.

Due to the fast development of Smart Antenna Systems, many research efforts have been devoted to hardware implementation of adaptive beamformer. Because of its strong interference rejection capability and simplicity, the Capon beamformer, also known as MVDR (Minimum Variance Distortionless Response) beamformer, has been the target for hardware implementation in several works. Dick and Harris performed a real-time QR decomposition-based Capon Beamformer implementation [35]. They provided a flexible and compact architecture for a real-time beamformer, together with their Matlab/Simulink design flow for heterogeneous architecture designs. Edman extensively investigated many alternative realizations for the Capon Beamformer and used their FPGA implementation in Channel Sounder application [36]. Liu et al, presented the Capon Beamformer implementation based on dichotomous coordinate descent iterations [41], instead of the popular QR Decomposition method, resulting in an area efficient realization. In addition, there exist many works on implementing an MVDR beamformer with RLS (Recursive Least Squares) adaptive algorithm [37].

As previously mentioned, Capon Beamformer suffers from the lack of robustness. Due to this drawback, any model errors could cause significant performance degradation, which limits its practical applications. Wang et al, presented an implementation of a robust adaptive beamformer in [38], namely Gershman's Beamformer [38], which has better performance than Capon Beamformer. It has been proven that the Robust Capon Beamformer implemented in our thermoacoustic imaging project is equivalent to Gershman's Beamformer [29], i.e., both algorithms produce the same weight vector. However the approach we adopted gives a simple way to eliminate the scaling ambiguity when estimating the SOI power and is also more computationally efficient [29]. Besides, hardware architecture of Gershman's Beamformer is not mentioned in [38]. On the other hand, major building blocks and architectures of our RCB implementation are illustrated in this thesis.

3.3.1 Implementation of Standard RCB

3.3.1.1 System block diagram

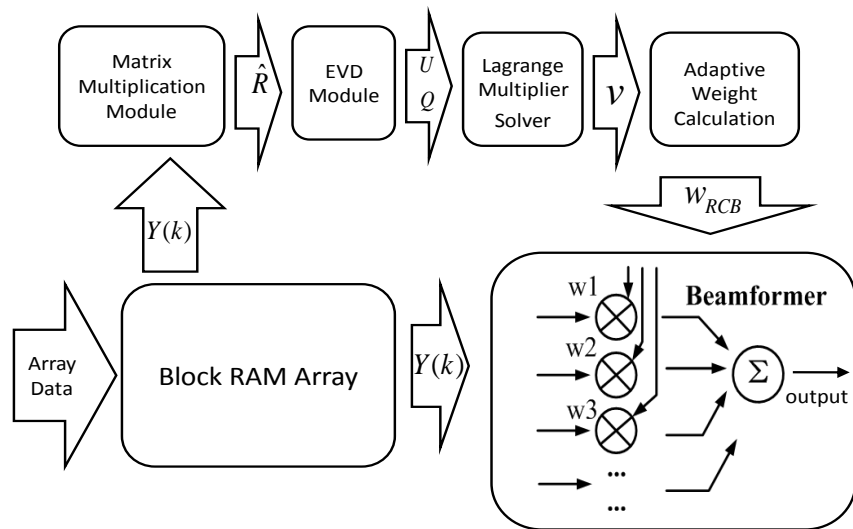


Figure 3-12. System Block Diagram

The system block diagram for hardware implementation of the Standard Narrowband RCB algorithm is shown in Figure 3-12. Array output data is fed into the Block Ram Array, and every two Block Ram store the real part and imaginary part of one channel of data respectively. Data is initially read from Block Ram Array into the Matrix Multiplication Module which computes sample covariance matrix. This matrix is used as input for Eigendecomposition Module. After eigen-values and eigen-vectors are computed the Lagrange Multiplier Solver module uses these terms to calculate the Lagrange multiplier based on an iterative method. The Lagrange multiplier is then utilized to determine adaptive weight vector. This weight vector generated is then applied to array output data to complete beamforming process.

3.3.1.2 Complex Multiply and Accumulate Unit

The pipelined architecture is adopted for realizing multiplication and accumulation of complex numbers. Guard bits are added in intermediate stages and accumulator stage to prevent overflow, while the final result is truncated to 18 bit fixed point representation giving sufficient accuracy. Several such modules are instantiated in a linear array fashion in order to parallelize the computation. The datapath of MAC module is illustrated in Figure 3-13 as below.

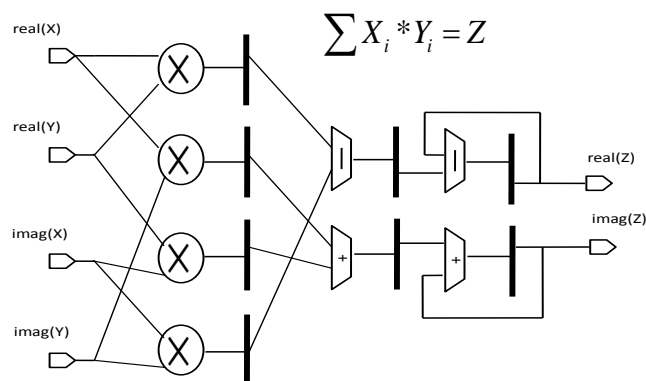


Figure 3-13. Datapath of Complex MAC Module

3.3.1.3 Extended Cyclic Jacobi Method

Cyclic Jacobi Method is a well-know numerical algorithm for eigenvalue decomposition of symmetric real-valued matrix [39][44]. To deal with complex-valued data, an extension of the Cyclic Jacobi Method is adopted to compute Eigen decomposition of a Hermitian Matrix [42]. The formulation is outlined as follow.

$$\mathbf{A}^0 = \mathbf{A} \quad \mathbf{A}^{k+1} = \mathbf{J}_{pq} \mathbf{A}^k \mathbf{J}_{pq}^* \quad (3-10)$$

\mathbf{A} is the original matrix, and \mathbf{A}^{k+1} is the matrix after k^{th} iteration. \mathbf{J}_{pq} is transformation matrix which eliminates off diagonal element in the p^{th} row and q^{th} column of \mathbf{A}^k . \mathbf{J}_{pq} can be decomposed into two matrix, inner matrix \mathbf{M}_{pq} and outer matrix \mathbf{R}_{pq} , as below:

$$\mathbf{J}_{pq} = \mathbf{R}_{pq} \mathbf{M}_{pq} \quad (3-11)$$

In which \mathbf{M}_{pq} has the form:

$$\mathbf{M}_{pq}(i, j) = \delta_{i,j} (i, j \neq p, q) \quad (3-12)$$

$$\mathbf{M}_{pq}(p, p) = e^{-j\beta_{pq}}, \quad \mathbf{M}_{pq}(q, q) = e^{j\beta_{pq}}$$

$$\beta_{pq} = \frac{1}{2} \arg[\mathbf{A}^k(p, q)]$$

While \mathbf{R}_{pq} has the form:

$$\mathbf{R}_{pq}(i, j) = \delta_{i,j} (i, j \neq p, q) \quad (3-12)$$

$$\mathbf{R}_{pq}(p, p) = \mathbf{R}_{pq}(q, q) = \cos \theta_{pq} \quad \mathbf{R}_{pq}(p, q) = -\mathbf{R}_{pq}(q, p) = \sin \theta_{pq}$$

$$\theta_{pq} = \frac{1}{2} \tan^{-1} \left(\frac{2\|\mathbf{A}^k(p, q)\|}{\mathbf{A}^k(q, q) - \mathbf{A}^k(p, p)} \right)$$

where $\delta_{i,j}$ is the Kronecker Delta and $\mathbf{A}^k(p, q)$ is the complex-valued off diagonal element in the p^{th} row and q^{th} column of \mathbf{A}^k , while $\arg[\mathbf{A}^k(p, q)]$ and $\|\mathbf{A}^k(p, q)\|$ are the angle and norm of $\mathbf{A}^k(p, q)$ respectively.

After multiplying both sides of \mathbf{A}^k by inner matrix \mathbf{M}_{pq} , $\mathbf{A}^k(p, q)$ and $\mathbf{A}^k(q, p)$ will become real numbers. Then multiplication of outer matrix \mathbf{R}_{pq} reduces these two off-diagonal elements to zero by plane rotation. During every transformation, two rows of elements of \mathbf{A}^k are updated with diagonal elements being $\mathbf{A}^k(p, p)$ and $\mathbf{A}^k(q, q)$, and off-diagonal elements being $\mathbf{A}^k(p, i)$ and $\mathbf{A}^k(q, i)$ ($i \neq p, q$). Both $\mathbf{A}^k(p, q)$ and $\mathbf{A}^k(q, p)$ are reduced to zero, as illustrated.

$$\mathbf{A}_{pp}^{k+1} = \frac{\mathbf{A}_{pp}^k + \mathbf{A}_{qq}^k}{2} + \sin(2\theta_{pq}) \|A_{pq}^k\| - \cos(2\theta_{pq}) \frac{\mathbf{A}_{pp}^k - \mathbf{A}_{qq}^k}{2} \quad (3-13)$$

$$\mathbf{A}_{qq}^{k+1} = \frac{\mathbf{A}_{pp}^k + \mathbf{A}_{qq}^k}{2} - \sin(2\theta_{pq}) \|A_{pq}^k\| + \cos(2\theta_{pq}) \frac{\mathbf{A}_{pp}^k - \mathbf{A}_{qq}^k}{2}$$

$$\mathbf{A}_{pq}^{k+1} = \mathbf{A}_{qp}^{k+1} = 0$$

$$\mathbf{A}_{pi}^{k+1} = \cos(\theta_{pq}) \mathbf{A}_{pi}^k e^{-j\beta_{pq}} - \sin(\theta_{pq}) \mathbf{A}_{qi}^k e^{j\beta_{pq}}$$

$$\mathbf{A}_{qi}^{k+1} = \sin(\theta_{pq}) \mathbf{A}_{pi}^k e^{-j\beta_{pq}} + \cos(\theta_{pq}) \mathbf{A}_{qi}^k e^{j\beta_{pq}} \quad i \neq p, q$$

A detailed derivation of the extended Cyclic Jacobi Method can be found in [42].

Datapath of EVD Module consists of a linear array of Processor Elements (PE), and is illustrated in Figure 3-14.

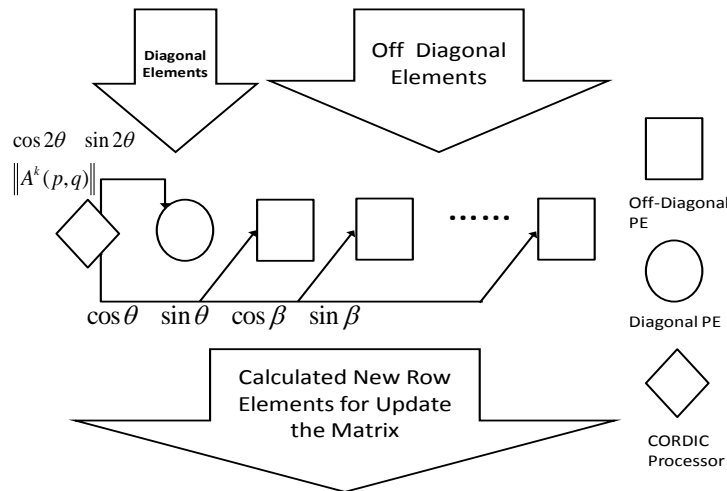


Figure 3-14. Datapath for Eigenvalue Decomposition Module

CORDIC processor [40] takes $A^k(p, q)$ from A^k , calculates the trigonometric functions of angle β_{pq} , rotation angle θ_{pq} and norm of $A^k(p, q)$, and feeds them to diagonal PE and off-diagonal PEs. The diagonal PE and off-diagonal PEs work in parallel to speed up computation. The whole datapath operates on the entire row of A^k at once. Datapath for CORDIC processor is shown in Figure 3-15. It contains two identical CORDIC units in order to evaluate the angles and calculate the trigonometric functions of β_{pq} , $2\theta_{pq}$ and θ_{pq} in an efficient and parallel way. Datapath for diagonal PE is illustrated in Figure 3-16, while datapath of off-diagonal PE is not included for brevity.

Datapath for calculating eigen-vectors is almost the same as that shown in Figure 3-14 but only with off-diagonal PEs, and takes the identity matrix as input and generates eigenvectors as output [44]. Based on experimental result, a total of 3 sweeps achieves sufficient accuracy for eigenvalues on a 4 by 4 complex-valued matrix. Due to the progressively small amplitude of off-diagonal elements, the evaluation of β_{pq} will become worse leading to poor accuracy of computations for eigen-vectors. However the whole algorithm is not very sensitive to the inaccuracy of eigenvectors, and still finds the adaptive weight vector with an acceptable accuracy.

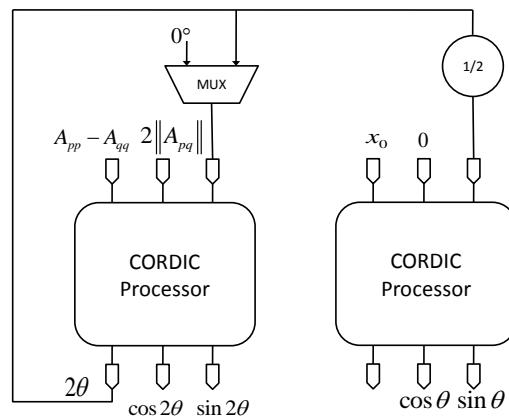


Figure 3-15. Datapath for CORDIC Processor

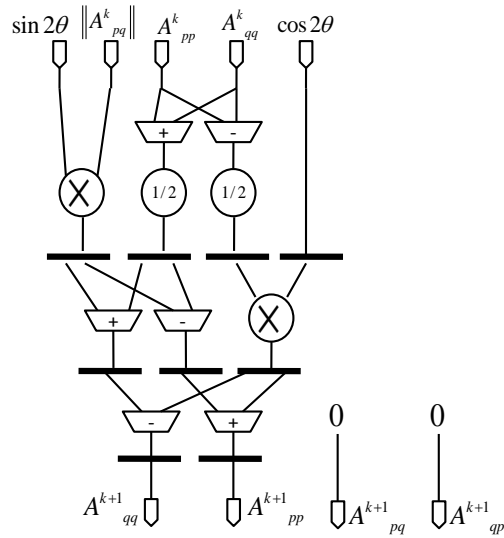


Figure 3-16. Datapath for Diagonal Processing Element

3.3.1.4 Lagrange Multiplier Solver

The Lagrange Multiplier is obtained by solving equation (3-7) iteratively. Many iterative root-finding algorithms can be applied here and we adopt the binary search method due to its simplicity and robustness. The number of iterations is a user-defined parameter. Datapath of the Lagrange multiplier solver is illustrated in Figure 3-17.

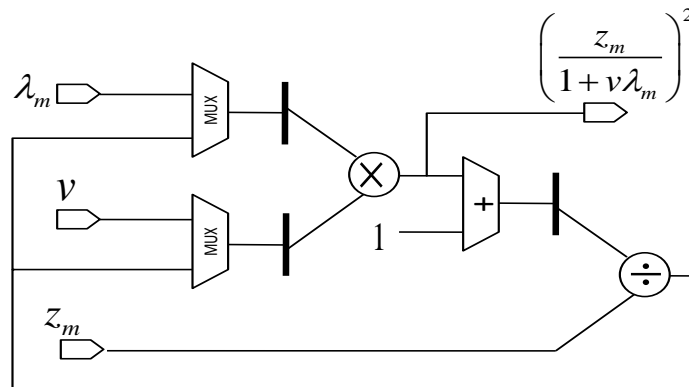


Figure 3-17. Datapath of Lagrange Multiplier Solver

The divider is based on CORDIC processor [40], and the multiplier is from Xilinx primitive. This datapath is timely shared by computations for M vector components. The

results are added together by an adder tree. The sum is taken by controller and compared to ε in equation (3-7). If the sum is larger than ε , then we take the upper half region as the solution region due to the monotonically decreasing property of the left side of equation (3-7) and perform the next iteration of binary search on this chosen region. Otherwise, we take the lower half region as the solution region and perform the next iteration of binary search on this chosen region. After a few number of iterations the Lagrange multiplier is found with an acceptable accuracy.

3.3.1.5 Adaptive Weight Calculation

From equation (3-9), we can see that in order to calculate adaptive weight vector, we need to compute $\hat{\mathbf{a}}_0$ and $\hat{\mathbf{R}}^{-1}\hat{\mathbf{a}}_0$. Developing individual datapaths for each computation is possible, but consumes more hardware resources. We therefore reformulate the computations for $\hat{\mathbf{a}}_0$ and $\hat{\mathbf{R}}^{-1}\hat{\mathbf{a}}_0$ to make resource sharing possible, as shown below:

$$\begin{aligned}
\hat{\mathbf{a}}_0 &= \left(\frac{\hat{\mathbf{R}}^{-1}}{v} + \mathbf{I} \right)^{-1} \bar{\mathbf{a}}_0 & (3-14) \\
&= \left(\frac{\mathbf{Q}^* \mathbf{U}^{-1} \mathbf{Q}}{v} + \mathbf{Q}^* \mathbf{Q} \right)^{-1} \bar{\mathbf{a}}_0 \\
&= \mathbf{Q} \begin{pmatrix} \frac{v\lambda_1}{v\lambda_1+1} & 0 & 0 & 0 \\ 0 & \frac{v\lambda_2}{v\lambda_2+1} & 0 & 0 \\ 0 & 0 & \dots & 0 \\ 0 & 0 & 0 & \frac{v\lambda_m}{v\lambda_m+1} \end{pmatrix} \mathbf{Q}^* \bar{\mathbf{a}}_0 \\
&= \mathbf{Q} \mathbf{P}_1 \bar{\mathbf{a}}_0
\end{aligned}$$

$$\begin{aligned}
\hat{\mathbf{R}}^{-1}\hat{\mathbf{a}}_0 &= \hat{\mathbf{R}}^{-1} \left(\frac{\hat{\mathbf{R}}^{-1}}{v} + \mathbf{I} \right)^{-1} \bar{\mathbf{a}}_0 & (3-15) \\
&= \left[\left(\frac{\hat{\mathbf{R}}^{-1}}{v} + \mathbf{I} \right) \hat{\mathbf{R}} \right]^{-1} \bar{\mathbf{a}}_0
\end{aligned}$$

$$\begin{aligned}
&= \left(\frac{Q^*Q}{v} + Q^*UQ \right)^{-1} \bar{a}_0 \\
&= Q \begin{pmatrix} \frac{v}{v\lambda_1+1} & 0 & 0 & 0 \\ 0 & \frac{v}{v\lambda_2+1} & 0 & 0 \\ 0 & 0 & \dots & 0 \\ 0 & 0 & 0 & \frac{v}{v\lambda_m+1} \end{pmatrix} Q^* \bar{a}_0 \\
&= QP_2 \bar{a}_0
\end{aligned}$$

The matrices P_1 and P_2 have the same form, both being the result of a multiplication of a diagonal matrix and Q^* , which simply results in a scaling of rows of Q^* . The matrices P_1 and P_2 are then multiplied by matrix Q . As a result, these computations can be performed by utilizing the Matrix Multiplication Module used in computing sample covariance matrix with additional control. This hardware resource sharing can save a significant amount of area in FPGA with the penalty of longer latency for computation.

3.3.1.6 FPGA implementation

The hardware implementation of the standard narrowband RCB algorithm is realized using a Xilinx Virtex-4 SX35 FPGA. In our realization, an 18 bit fixed-point representation is adopted which provides sufficient accuracy for present application. The array output consists of 4 channels of complex-valued data, and the number of snapshots used for beamforming is 32. The resource utilization for our application is listed in Table 3-1.

Table 3-1. Resource Utilization for RCB Implementation

Resource	Used	Available	Utilization
Slices	14978	15360	97%
FF	13420	30720	43%
LUTs	23246	30720	75%
BRAM	41	192	21%
DSP48	192	192	100%

The latency for one sweep in EVD computation for a 4 by 4 complex-valued matrix is around 540 cycles. With a total of 3 sweeps, the overall latency of RCB algorithm is approximately 5485 cycles, which can be further improved by exploiting more parallelism and reducing control overhead. Since this design is running at a clock speed of 100MHz, roughly 54.85 microseconds delay is expected for one update of adaptive weights. Compromises have been made in choosing between triangular systolic array and linear array processor architecture for EVD core in order to save hardware resources at the expense of increased latency and control complexity.

3.3.2 Implementation of Wideband RCB

In wideband RCB algorithm implementation, the input signal is the real-valued data, and the signal processing operations involved are all real-valued computations. The signal alignment and amplitude compensation are performed on the host PC, and the time-delayed, compensated data is then transferred to the FPGA by the PCI interface and processed by the modified wideband RCB algorithm. Major differences between the original narrowband RCB algorithm and the modified wideband RCB algorithm lie in the eigenvalue decomposition step, although there are other minor differences in other computational steps. In the standard RCB, the covariance matrix is a complex hermitian matrix, while in the modified wideband RCB, the covariance matrix is a real symmetric matrix. As a result, the eigenvalue decomposition module in the wideband RCB implementation is simply based on the cyclic Jacobi method. In the wideband RCB implementation, the multiply and accumulate operation is based on the real number, and therefore is much simpler than MAC operation in the narrowband RCB implementation.

3.3.2.1 Cyclic Jacobi Method for Eigendecomposition

Cyclic Jacobi Method is a well-know numerical algorithm used to calculate eigenvalue decomposition of symmetric real-valued matrix [39][44]. It is robust and the convergence is guaranteed. The formulation is outlined as follows:

$$\mathbf{A}^0 = \mathbf{A} \quad \mathbf{A}^{k+1} = \mathbf{J}_{pq} \mathbf{A}^k \mathbf{J}_{pq}^* \quad (3-16)$$

where \mathbf{A} is the original matrix, and \mathbf{A}^{k+1} is the resulting matrix after k^{th} iteration. \mathbf{J}_{pq} is the plane rotation matrix which eliminates off-diagonal element in the p^{th} row and q^{th} column of \mathbf{A}^k , thus has the form in equation (3-17).

$$\begin{aligned} \mathbf{J}_{pq}(i, j) &= \delta_{i,j} \quad (i, j \neq p, q) \\ \mathbf{J}_{pq}(p, p) &= \mathbf{J}_{pq}(q, q) = \cos \theta_{pq} \\ \mathbf{J}_{pq}(p, q) &= -\mathbf{J}_{pq}(q, p) = \sin \theta_{pq} \\ \theta_{pq} &= \frac{1}{2} \tan^{-1} \left(\frac{2\mathbf{A}^k(p, q)}{\mathbf{A}^k(q, q) - \mathbf{A}^k(p, p)} \right) \end{aligned} \quad (3-17)$$

where $\delta_{i,j}$ is the Kronecker Delta and $\mathbf{A}^k(p, q)$ is off-diagonal element in the p^{th} row and q^{th} column of \mathbf{A}^k . After multiplying both sides of \mathbf{A}^k by rotation matrix \mathbf{J}_{pq} , two rows of elements of \mathbf{A}^k are updated with diagonal elements $\mathbf{A}^k(p, p)$ and $\mathbf{A}^k(q, q)$, and off-diagonal elements $\mathbf{A}^k(p, i)$ and $\mathbf{A}^k(q, i)$ ($i \neq p, q$). Both $\mathbf{A}^k(p, q)$ and $\mathbf{A}^k(q, p)$ are reduced to zero, as illustrated below.

$$\begin{aligned} \mathbf{A}_{pp}^{k+1} &= \frac{\mathbf{A}_{pp}^k + \mathbf{A}_{qq}^k}{2} + \sin(2\theta_{pq}) \mathbf{A}_{pq}^k - \cos(2\theta_{pq}) \frac{\mathbf{A}_{pp}^k - \mathbf{A}_{qq}^k}{2} \\ \mathbf{A}_{qq}^{k+1} &= \frac{\mathbf{A}_{pp}^k + \mathbf{A}_{qq}^k}{2} - \sin(2\theta_{pq}) \mathbf{A}_{pq}^k + \cos(2\theta_{pq}) \frac{\mathbf{A}_{pp}^k - \mathbf{A}_{qq}^k}{2} \\ \mathbf{A}_{pq}^{k+1} &= \mathbf{A}_{qp}^{k+1} = 0 \\ \mathbf{A}_{pi}^{k+1} &= \cos(\theta_{pq}) \mathbf{A}_{pi}^k - \sin(\theta_{pq}) \mathbf{A}_{qi}^k \end{aligned} \quad (3-18)$$

$$A_{qi}^{k+1} = \sin(\theta_{pq}) A_{pi}^k + \cos(\theta_{pq}) A_{qi}^k \quad i \neq p, q$$

A detailed derivation of Cyclic Jacobi Method can be found in [39]. Datapath of EVD Module consists of a linear array of Processor Elements (PE), and is illustrated in Figure 3-18.

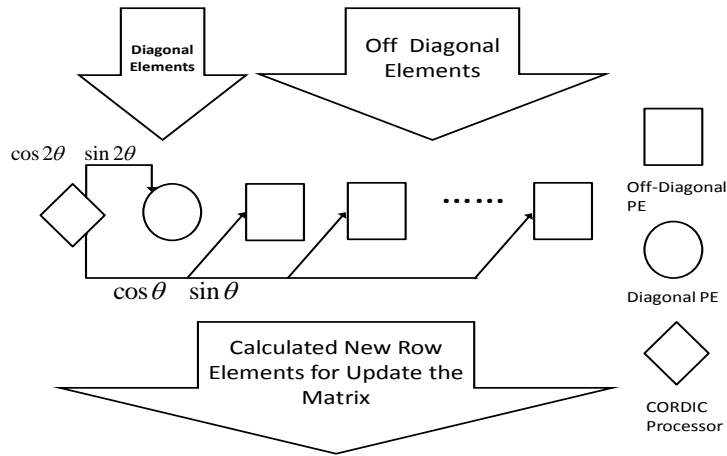


Figure 3-18. Datapath for Eigenvalue Decomposition Module

CORDIC processor [40] takes $A^k(p, q)$ from A^k , calculates the trigonometric functions of rotation angle θ_{pq} , and feeds them to diagonal PE and off-diagonal PEs. The diagonal PE and off-diagonal PEs work in parallel to speed up computation. The whole datapath operates on entire row of A^k at once. Datapath for CORDIC processor is shown in Figure 3-19. It contains two identical CORDIC units in order to calculate the trigonometric functions of $2\theta_{pq}$ and θ_{pq} in parallel. Datapath for diagonal PE is illustrated in Figure 3-20, while the datapath of off-diagonal PE is illustrated in Figure 3-21.

Datapath for calculating eigen-vectors is nearly the same as that shown in Figure 3-18 but only with off-diagonal PEs, and takes the identity matrix as input and generates eigen-vectors as output [44]. Based on experimental result, a total of 4 sweeps achieves sufficient accuracy for eigen-values and eigen-vectors.

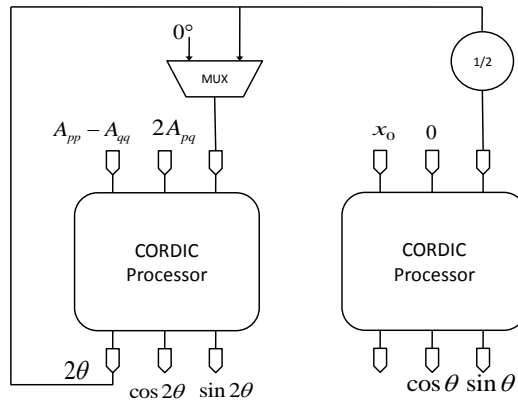


Figure 3-19. Datapath for CORDIC Processor

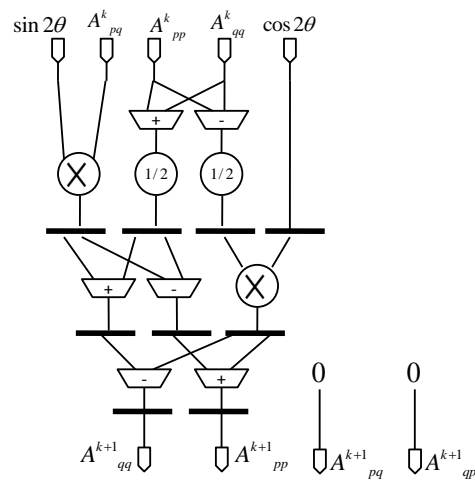


Figure 3-20. Datapath for Diagonal Processing Element

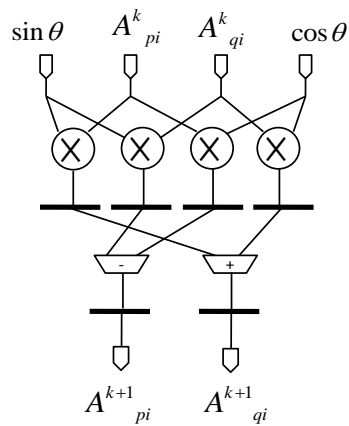


Figure 3-21. Datapath of Off-Diagonal Processing Element

3.3.2.2 FPGA implementation of wideband RCB

The hardware implementation of wideband RCB algorithm is realized using a Xilinx Virtex-4 SX35 FPGA. The algorithm simulation is performed using MATLAB, and the implementation is accomplished by VHDL programming. In our realization, an 18 bit fixed-point representation is adopted which provides sufficient accuracy for present application. The array output consists of 8 channels of real-valued data, and the number of snapshots used for beamforming is 32. The resource utilization for our application is listed in Table 3-2.

Table 3-2.Resource Utilization for Wideband RCB Implementation

Resource	Used	Available	Utilization
Slices	10674	15360	69%
FF	9377	30720	30%
LUTs	17042	30720	55%
BRAM	24	192	12%
DSP48	83	192	43%

The latency for one sweep in EVD computation for an 8 by 8 real-valued matrix is around 2312 cycles, which can be further reduced by eliminating more control overhead. With a total of 4 sweeps, the overall latency of RCB algorithm is approximately 11374 cycles, which can be further improved by exploiting more parallelism. Since this design is running at a clock speed of 80MHz, roughly 140 microseconds delay is expected for one update of adaptive weight. Compromises have been made in choosing between triangular systolic array and linear array processor architecture for EVD core in order to save hardware resources at the expense of increased latency and control complexity.

CHAPTER 4
EXPERIMENTAL RESULTS OF THERMOACOUSTIC IMAGING SYSTEM

4.1 Experimental Step-up of TAI System

4.1.1 Introduction

The experimental setup is built to conduct proof-of-principle research for our thermoacoustic imaging system. It can generate high peak power, short duration microwave pulse used to illuminate phantom body, pick up the emitted thermoacoustic signal by transducer subsystem, digitize and record the signal by Data Acquisition subsystem (DAQ). The system block diagram is showed in Figure 4-1. The whole system can be divided into three subsystems, including high power subsystem, transducer array subsystem and data acquisition subsystem, which are described in details as follow.

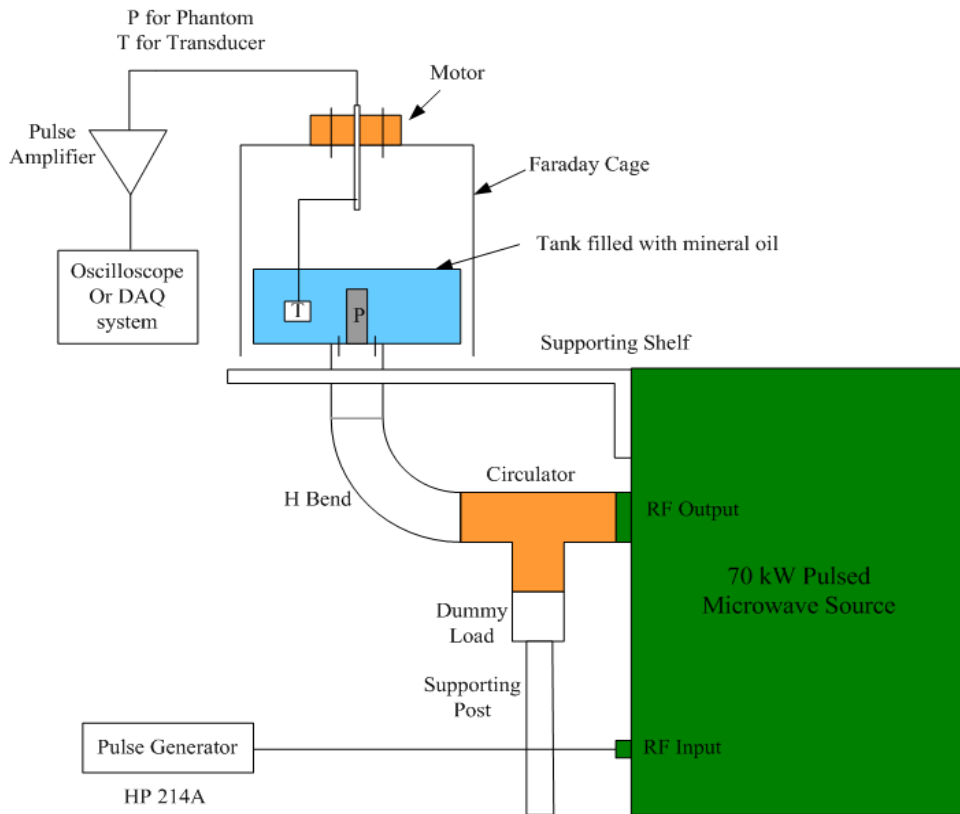


Figure 4-1. TAI System Block Diagram

4.1.1.1 High Power Subsystem

High power subsystem operates to generate high peak power microwave pulse, feed it into experimental tank and provide reflection protection for microwave source. Major components involved are pulsed microwave source, pulse generator, circulator, dummy load, H bend and supporting table. The real system is showed in Figure 4-2 below.

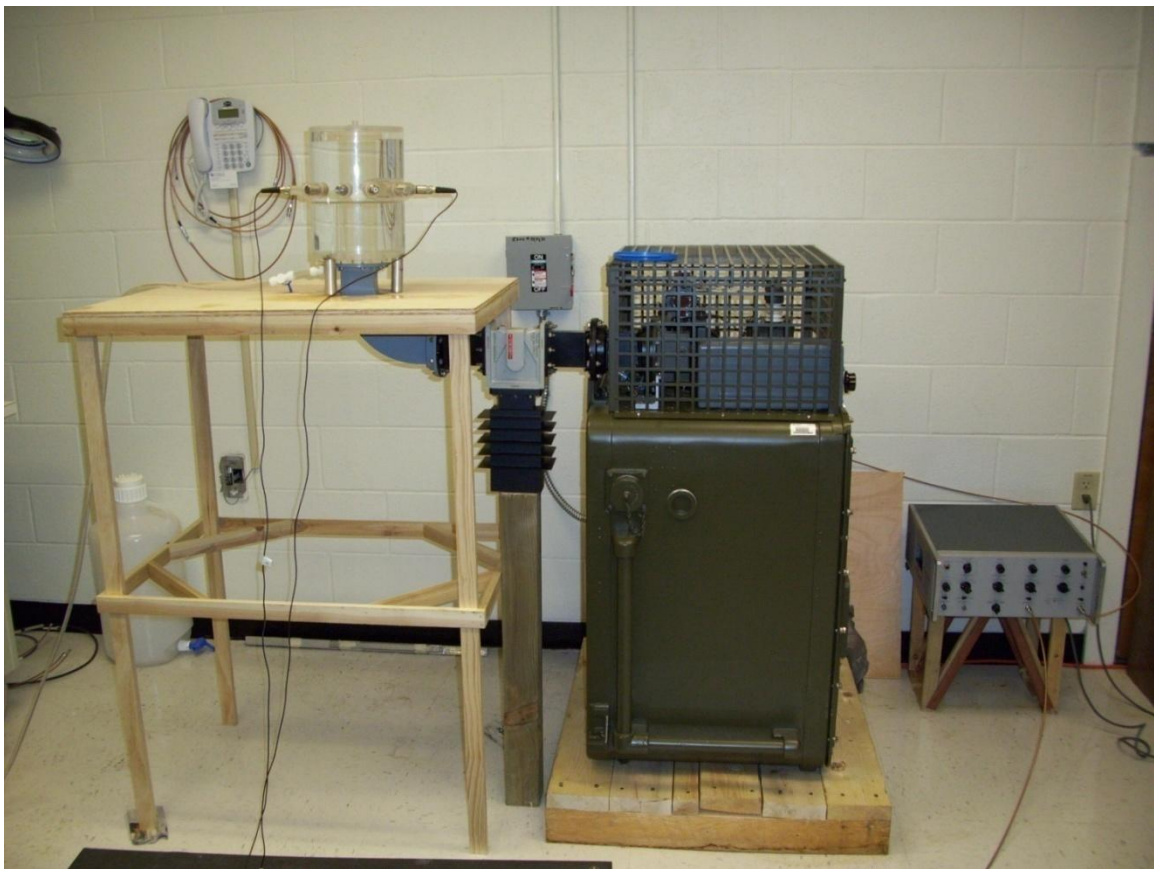


Figure 4-2. High Power Subsystem. Photo Courtesy of Xin Guan.

HP 214A pulse generator [45] is used to generate the trigger signal for pulsed microwave source. The output signal should be a pulse with peak voltage 200 V. The pulse repetition rate could be adjusted according to specific application requirement in the range of 30 Hz to 1100 Hz, or even manual mode. It can operate in several trigger

modes, including manual trigger, exterior trigger and internal trigger. In our experiments, we set it to internal trigger mode and 100 Hz pulse repetition rate. The control panel in our configuration looks like Figure 4-3 below.



Figure 4-3. Control Panel of Pulse Generator. Photo Courtesy of Xin Guan.

The output signal from pulse generator is also used as the trigger signal to synchronize data acquisition (a certain amount of delay is inserted) after firing the electromagnetic illumination. Because the amplitude of trigger signal is 200 V, a voltage attenuator with 20 dB attenuation at least is used to reduce the voltage to 2 V and feed into the external trigger port on digitizer card.

The pulsed microwave source is from Radio-Research Instrument Co., and the part number is 12-1-21MOD [45]. 3-phase electricity with 120 V nominal voltage is used to power the equipment. If operated at its maximum capability, this microwave source is capable of supplying 0.75 μ s pulse at repetition rate of 1100 Hz and peak power of 120 kW. The fundamental frequency of microwave pulse is fixed around 3GHz. Pulse repetition rate can be adjusted by setting the HP pulse generator to an appropriate value like 100 Hz. The output power could be controlled by the high voltage applied inside the system, which can be changed by the knob on the front control panel. Pulse

duration is fixed to 0.75 us, which can only be changed by replacing the pulse forming network circuit inside the equipment. The operational status is summarized in Figure 4-4 below, in which the red part indicates the nominal operation condition for our experiments.

APPROXIMATE PULSE GENERATOR AND MODULATOR HIGH VOLTAGE SETTINGS

PRF & POWER		PULSE GENERATOR SETTINGS												MODULATOR METER READINGS		
PRF (Hz)	PEAK POWER LEVEL (kW)	TRIG MODE	INT REP RATE	REP RATE VERN.	NORM / GATED	PULSE POS.	PULSE POS. VERN.	PULSE ADV / DELAY	PULSE WIDTH	PULSE WIDTH VERN.	PULSE AMPL.	PULSE AMPL. VERN.	PULSE OUTPUT	SET HIGH VOLT. ADJUST FOR kV	TYPICAL MAG. CURRENT mA	TYPICAL RECT. CURRENT mA
1100	120	INT	.1-1	2:00	NORM	0-1	7:00	DELAY	.05-1	1:00	100	7:00	+	4.8	17.0	90
1100	75	INT	.1-1	2:00	NORM	0-1	7:00	DELAY	.05-1	1:00	100	7:00	+	3.2	8.5	-55
1100	50	INT	.1-1	2:00	NORM	0-1	7:00	DELAY	.05-1	1:00	100	7:00	+	2.8	5.5	45
1100	25	INT	.1-1	2:00	NORM	0-1	7:00	DELAY	.05-1	1:00	100	7:00	+	2.2	3.0	40
100	120	INT	.01-1	2:00	NORM	0-1	7:00	DELAY	.05-1	1:00	100	7:00	+	5.1	2.0	10
100	75	INT	.01-1	2:00	NORM	0-1	7:00	DELAY	.05-1	1:00	100	7:00	+	3.5	1.0	7
100	50	INT	.01-1	2:00	NORM	0-1	7:00	DELAY	.05-1	1:00	100	7:00	+	2.8	0.5	5
100	25	INT	.01-1	2:00	NORM	0-1	7:00	DELAY	.05-1	1:00	100	7:00	+	2.2	0.0	3
30	120	INT	.01-1	11:00	NORM	0-1	7:00	DELAY	.05-1	1:00	100	7:00	+	5.5	0.0	5
30	75	INT	.01-1	11:00	NORM	0-1	7:00	DELAY	.05-1	1:00	100	7:00	+	3.5	0.0	3
30	50	INT	.01-1	11:00	NORM	0-1	7:00	DELAY	.05-1	1:00	100	7:00	+	2.8	0.0	0
30	25	INT	.01-1	11:00	NORM	0-1	7:00	DELAY	.05-1	1:00	100	7:00	+	2.2	0.0	0
MAN	120	EXT	N/A	N/A	NORM	100-1K	2:00	DOUBLE PULSE	* 1-10	1:00	100	7:00	+	5.5	0.0	0
MAN	75	EXT	N/A	N/A	NORM	100-1K	2:00	DOUBLE PULSE	* 1-10	1:00	100	7:00	+	3.5	0.0	0
MAN	50	EXT	N/A	N/A	NORM	100-1K	2:00	DOUBLE PULSE	* 1-10	1:00	100	7:00	+	2.8	0.0	0
MAN	25	EXT	N/A	N/A	NORM	100-1K	2:00	DOUBLE PULSE	* 1-10	1:00	100	7:00	+	2.2	0.0	0

Figure 4-4. Summary of Operational Conditions

In real operation, we set the high voltage approximately to 2.0 kV, thus generating peak power less than 25 kW in order to keep radiation level as low as necessary based on safety concern. The columns named Typical Magnetron Current and Typical Rectifier Current are two indicators of output power level on the front control panel. Due to the low power operational condition, both of the indicators are approaching zero.

Because of mismatch of impedance at the power feeding interface between experimental tank and H bend, part of the input power will be reflected back toward power source, which is harmful for the equipment. The circulator is inserted between H bend and power source, and serves as reflection protection device. The reflected power will be directed to the dummy load and absorbed locally.

4.1.1.2 Transducer array subsystem

The transducer in usage is the unfocused immersion transducer from Panametrics NDT, model number V303-SU, which is showed in Figure 4-5 below. The center frequency is around 1 MHz, and the 6 dB bandwidth is 0.6 MHz. The impulse response lasts for nearly 4 us [46].



Figure 4-5. Transducer. Photo Courtesy of Xin Guan.

In order to form a transducer array, a motor-driven rotational stage is used together with one transducer to simulate a circular transducer array by rotating the single transducer to different circular positions during data acquisition process. This method is simple and economically efficient, but needs more time to collect data

compared with real transducer array. The schematic is in Figure 4-6. The front view is on the left while the top view is on the right. The orange part is the step motor fixed on the top of the aluminum fielding box. The mechanical arm punches through the motor, connects the transducer and serves as the rotational stage. The blue part represents experimental tank filled with mineral oil. Phantom sits in the middle of the tank, which stays on the top of H bend. Together with Figure 4-1, we can find that the relative positioning between phantom and transducer trajectory is not fixed during different rounds of experiment. The motor and transducer system is attached to the shielding box, while the experimental tank and phantom is fixed to H bend. Every time we take off the shielding box, change phantom and put back the shielding box, we can not exactly recover the previous positioning of the shielding box. That is one of major drawbacks for current transducer array subsystem. The direct consequence of this alignment issue is that the position of phantom in our final images is not consistent, although the shape is the same.

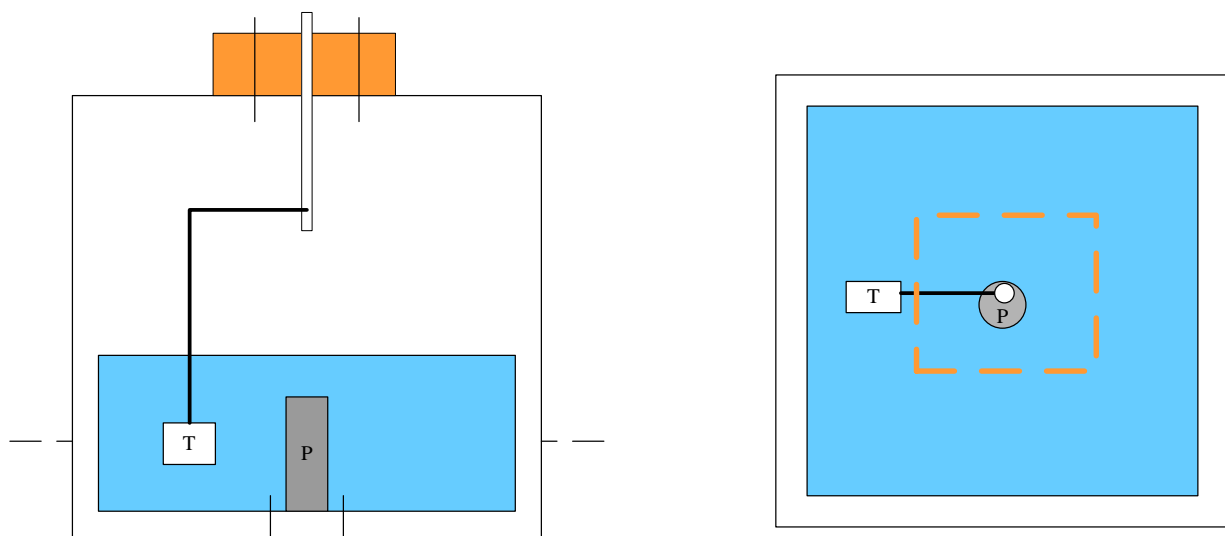


Figure 4-6. Motor and Transducer System

In our experiments, the transducer is swept along a circle with resolution of 3 degree, meaning total 120 scanning positions. At every circular position, high power system launches multiple microwave pulses and generates the same number of thermoacoustic responses, which are picked up by transducer and averaged and stored by DAQ system. After scanning the current position, motor rotates 3 degree to the next position and performs data collection at that position. In doing so, the simulated transducer array can collect data as if there were 120 transducers collecting data at the same time. The scanning schematic is showed in Figure 4-7 below.

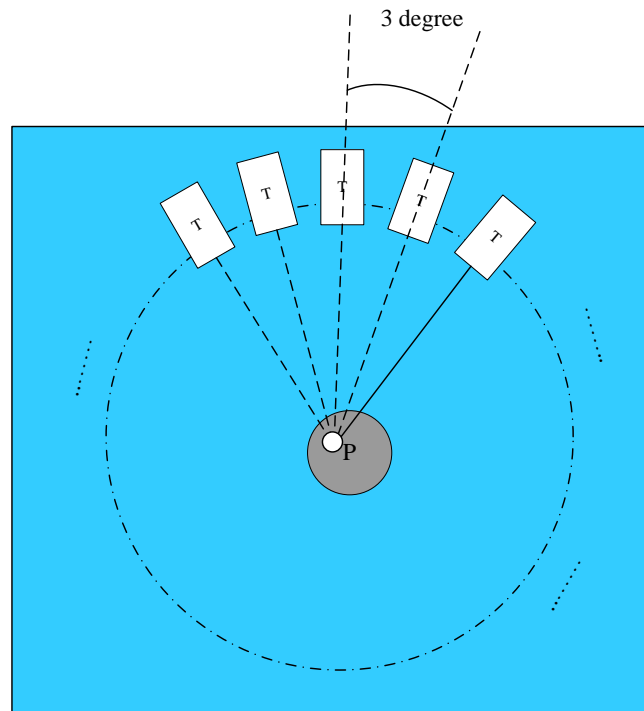


Figure 4-7. Scanning Schematic

4.1.1.3 DAQ subsystem

DAQ subsystem performs two functions, signal conditioning and data acquisition. Thermoacoustic signal is deeply embedded in noisy background including amplifier noise (especially with large amplification gain like 60 dB) and strong interference signals

such as EMI (Electromagnetic Induced) signal. First, the signal coming from transducer needs to be amplified and filtered, which is accomplished by the pulser/receiver equipment. Then the outcome has to be digitized by digitizer card, and averaged multiple times to increase SNR (Signal to Noise Ratio). At last, averaged signal can be recorded in data file, which will be utilized subsequently to perform imaging. The schematic of DAQ subsystem is showed in Figure 4-8 below.

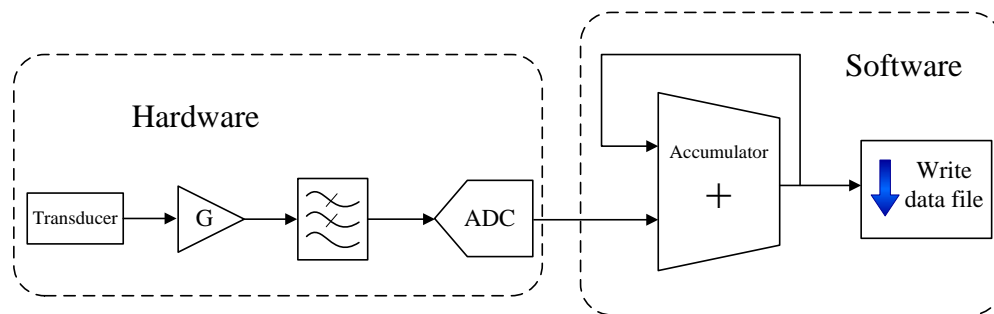


Figure 4-8. DAQ Subsystem Schematic

The pulser/receiver in usage is Olympus Panametrics-NDT 5800. The module operates in external pulser mode in order to solely utilize receiver module. The high pass filter cutoff frequency is set to 1 kHz, and the low pass filter cutoff frequency is set to 10 MHz. The amplifier gain is set to 60 dB, maximum allowable value, to amplify thermoacoustic signal as large as possible [47]. The operating parameters are displayed in Figure 4-9 below.



Figure 4-9. Pulser/Receiver Operating Parameters. Photo Courtesy of Xin Guan.

The digitizer card in usage is a NI PXI 5122 digitizer hosted in NI PXI box. It can work from 1 MSample/s to 100 MSample/s with 14 bit resolution on two ADC channels [48]. There is a software control panel embedded in the VI, which can be used to instantiate the digitizer in LabVIEW program. In the panel, you can set the operating parameters for application. The general setting for digitizer card in our experiments can be found in Figure 4-10 below.

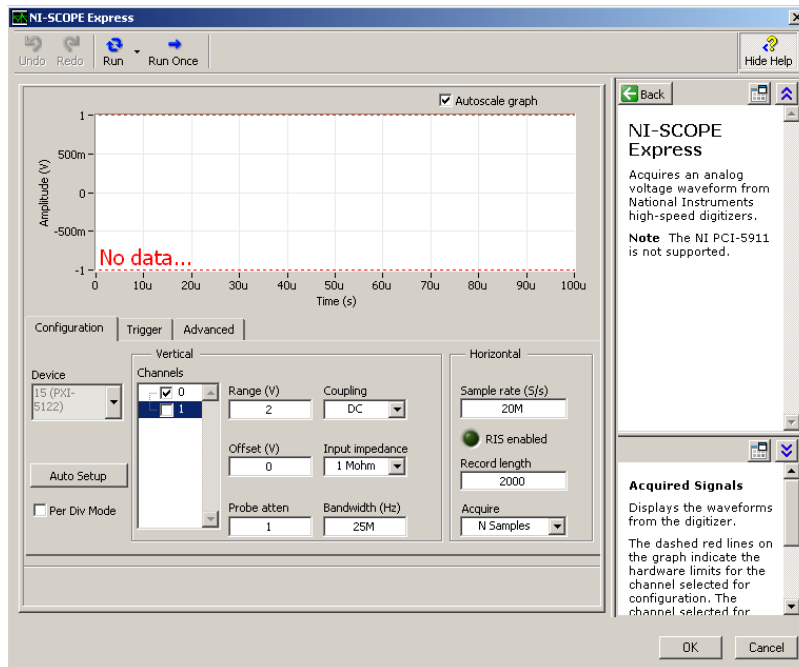


Figure 4-10. Configuration for NI 5122 Digitizer

In the configuration above, channel 0 has been selected for data acquisition. Input range is set to 2 V, no offset voltage. DC coupling is chosen to directly sample the entire waveform. High input impedance is set to capture the most part of signal. In this particular setting, 20 MSample/s sampling rate is taken with record length 2000 samples, corresponding to 10 us in time and 15 mm in distance, which covers the entire phantom area. In some experiments, if the phantom body is large, you need to set record length large enough to make sure you collect the generated thermoacoustic

A LabVIEW program was developed to coordinate between digitizer, motor control module, average functionality and data file generation. The control panel of the LabVIEW program is in Figure 4-12 below.

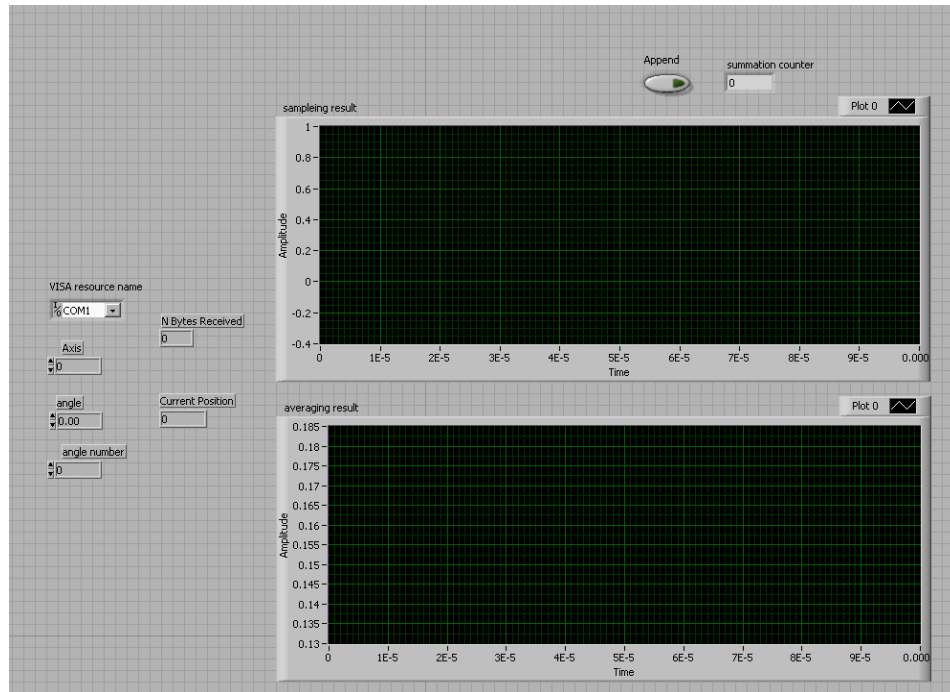


Figure 4-12. Control Panel

The angle indicator tells the current position of transducer, while the summation counter shows current averaging times. The top window displays sampled signal in real time, while the bottom window shows current averaged result. The data file will be generated for every transducer position, and can be loaded into matlab for further processing.

4.2 Thermoacoustic Signal Generation Experiment

In previous section, experimental setup of our TAI system is introduced, which consists of high power subsystem, transducer array subsystem and data acquisition subsystem. Using the system described earlier, we did the initial experiments to confirm the feasibility of thermoacoustic signal generation. In this initial experiment, we used the

old cylindrical tank with a bulk of phantom. The transducer was hung from the top surface of the tank in order to have better reception of acoustic signal. The important issue was that mineral oil should be used to fill the tank as bath material instead of distilled water [8], which has larger attenuation for microwave radiation. The experimental tank together with phantom and transducer is showed in Figure 4-13.

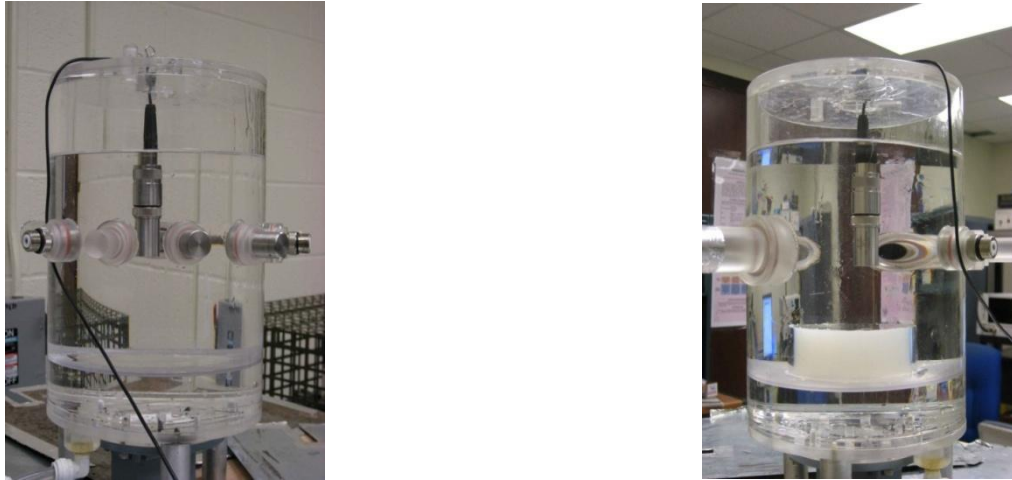


Figure 4-13. Tank without phantom (left), Tank with phantom (right). Photo Courtesy of Xin Guan.

Comparative studies have confirmed the source of acoustic signal, one experiment without phantom and the other experiment with phantom as depicted by Figure 4-13. The relative positioning between transducer and phantom is showed in Figure 4-14.

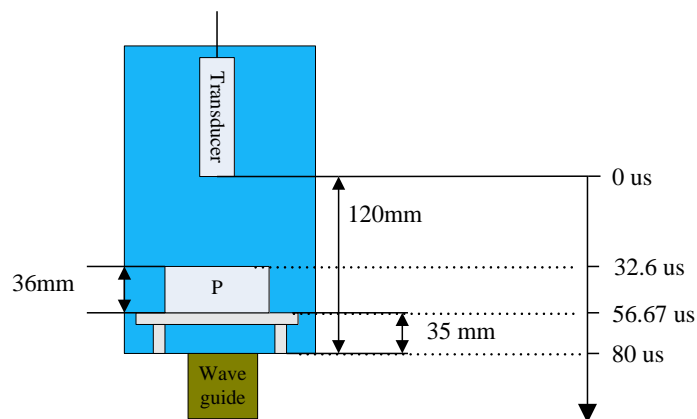


Figure 4-14. Relative Positions between Transducer and Phantom

Distance is converted to time-of-flight by sound speed 1.5 mm/us [49]. The signal generated by the top surface of phantom should arrive at transducer around 32.6 us, and the signal generated by the bottom surface of phantom should arrive at transducer around 56.6 us. This signal should be corrupted by the signal generated by the table surface. Acoustic signal generated in waveguide should arrive at transducer around 80 us. Due to the inaccuracy in measurements, estimates above are allowed to have several us deviation. Low frequency signal generated inside phantom body was filtered out by transducer. Thermoacoustic signal generated in this configuration is showed in Figure 4-15, which is the summation of recorded acoustic signal 16000 times instead of averaging.

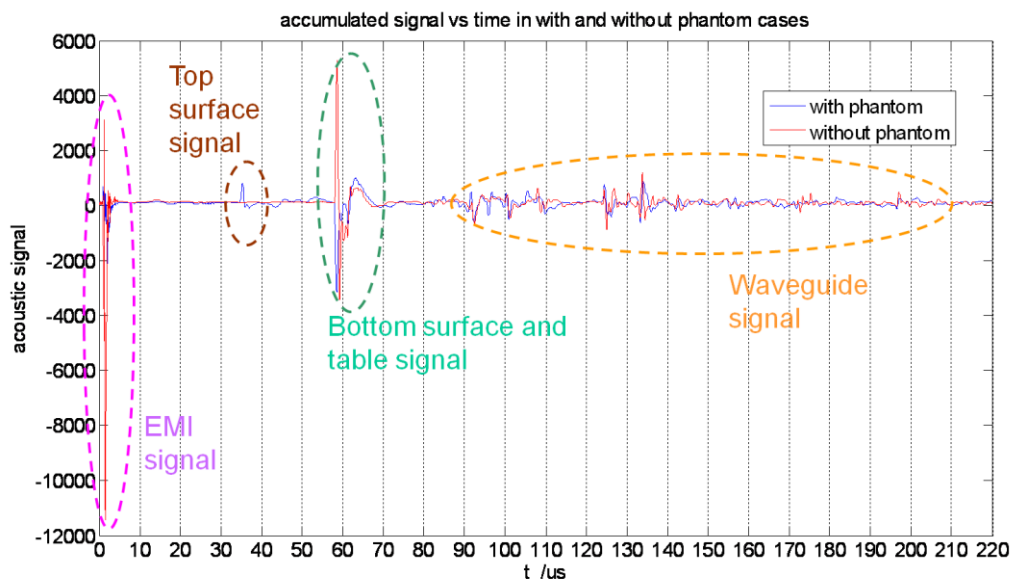


Figure 4-15. Thermoacoustic Signal in the First Experiment

In this initial experiment, the delay in data acquisition has not been inserted, and therefore the EMI signal appeared at the beginning of data sequence. The signal from the top surface of phantom was located around 35 us, while the signal from the bottom surface of phantom was located around 58.6 us, which are in good agreement with

previous time-of-flight analysis. To be specific, the signal appeared around 55 μs in experiment without phantom is the thermoacoustic signal generated by the supporting table, while the signal appeared around 55 μs in experiment with phantom is the thermoacoustic signal generated by the bottom surface of phantom loaded with the supporting table. The signal generated inside waveguide arrived near 82 μs as it was supposed to be [50]. A zoom-in view of above picture is showed in Figure 4-16, which mainly focuses on signal generated by the top and bottom surface of phantom.

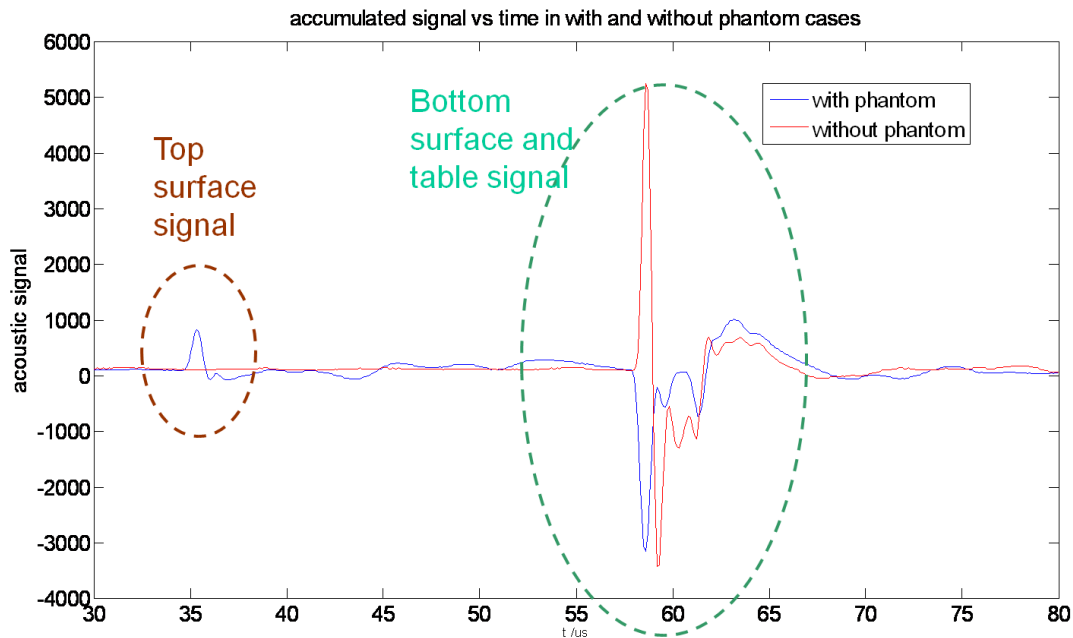


Figure 4-16. Zoom-in View of the Thermoacoustic Signal

It can be seen clearly that the signal existed when phantom was in the tank, while it disappeared when phantom was outside the tank, which confirmed that it was the thermoacoustic signal generated by the top surface of phantom. In order to prove the repeatability of the above experimental result, two more experiments have been conducted with same operating conditions. Pictures of thermoacoustic signal generated are showed in Figure 4-17 and Figure 4-18 respectively.

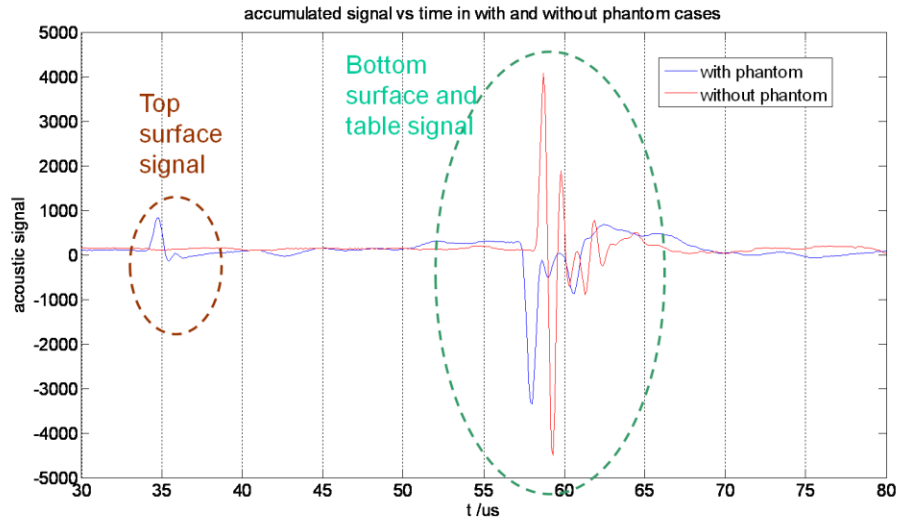


Figure 4-17. Thermoacoustic Signal in the Second Experiment

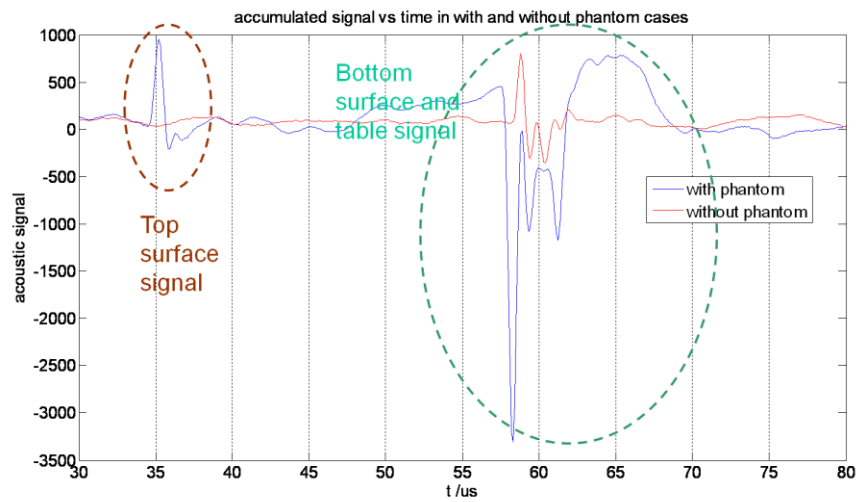


Figure 4-18. Thermoacoustic Signal in the Third Experiment

As can be seen from pictures above, thermoacoustic signal generated from the top surface of phantom repeatedly showed up, which further confirmed that the signal studied was the thermoacoustic signal generated by phantom.

4.3 Thermoacoustic Imaging Experiment

The initial experimental setup has several drawbacks. First, transducer was hung from the top of the tank, which can only be used to receive acoustic signal in one

direction, while in real imaging operation a transducer array is needed to collect signal from different directions. Second, the old cylinder tank is too small to allow the rotation of mechanical arm used in transducer array subsystem described in Chapter 3. We need a larger tank to make room for all circular positions transducer will stay. Third, the phantom is a bulk of material which has higher conductivity. As a result, only the thermoacoustic signal generated at the boundary can be detected and recorded. We need to build new phantom with bulk of background material which has lower conductivity and real target embedded inside background material which has higher conductivity in order to perform imaging. Based on these considerations, a new experimental tank has been made to accommodate phantom and transducer array, which is showed in Figure 4-19.



Figure 4-19. New Experimental Tank. Photo Courtesy of Xin Guan.

The tank can be fixed on the top of H bend, while phantom can be put at the center of the tank. New set of phantoms have been made to perform comparative studies. The background material is a cylinder with 30 mm in diameter and 40 mm in height, which consists of only distilled water and gelling agent. The targets are made into very slim cylinders embedded in background with 2 mm, 4 mm and 6 mm in

diameter and same height as background, consisting of 15% salt and gelling agent. Different sizes of targets are used to test the spatial resolution of our imaging system. The schematic of new phantom is showed in Figure 4-20.

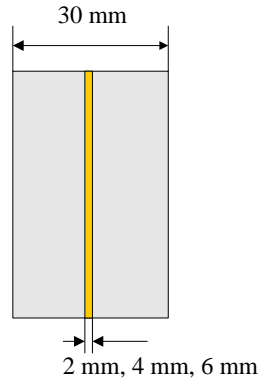


Figure 4-20. Schematic of the phantom

Thermoacoustic signals received at three circular positions during experiment, such as 0 degree, 120 degree and 240 degree, are displayed in Figure 4-21.

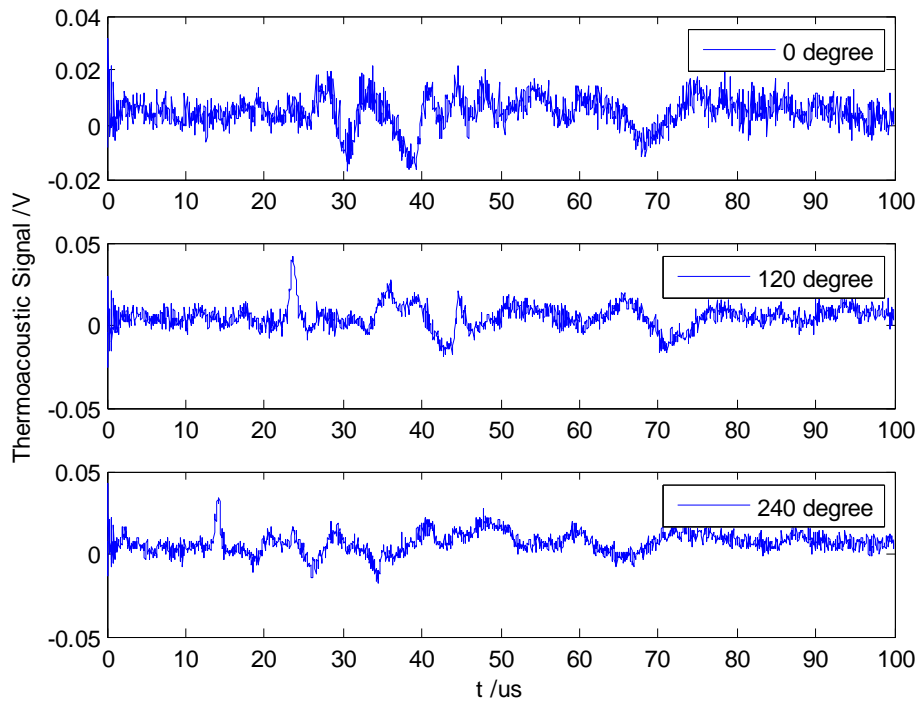


Figure 4-21. Thermoacoustic signals at 0, 120, 240 degree

4.4 Imaging Results

In order to perform comparison, different imaging algorithms, such as RCB, Standard Capon Beamforming (SCB) and Delay and Sum (DAS), are applied to thermoacoustic data collected from different phantom samples. The first set of images is constructed using data from phantom with 4 mm diameter, 15% salt target material.

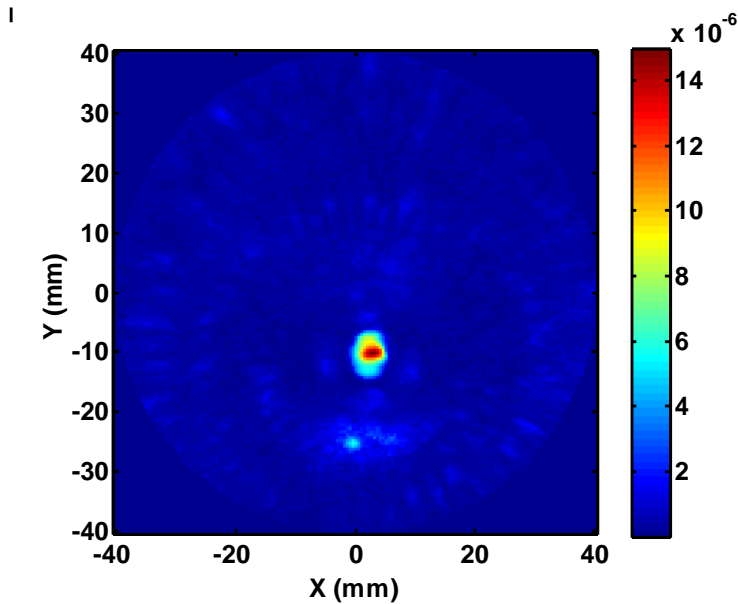


Figure 4-22. Imaging Result with 4mm 15% salt phantom using RCB

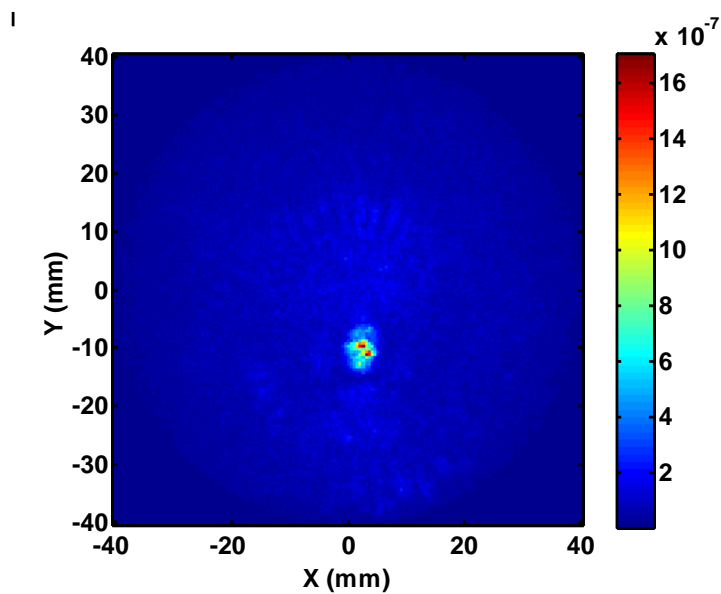


Figure 4-23. Imaging Result with 4mm 15% salt phantom using SCB

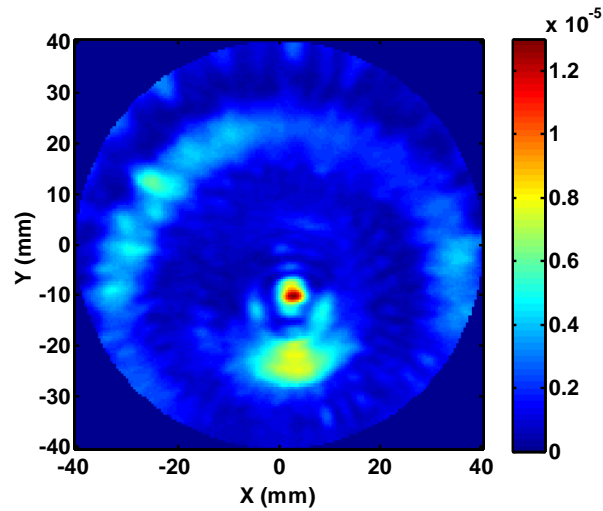


Figure 4-24. Imaging Result with 4mm 15% salt phantom using DAS

It is noticed that the target image obtained by SCB is smaller and isolated, while the image acquired from RCB is better having smoother boundary and clean background. On the other hand, the image from DAS is very noisy with many imaging artifacts. Actually RCB algorithm works between SCB and DAS algorithms. If the parameter ε in RCB is large, the result is more close to DAS. Otherwise, the result is more close to SCB. RCB results from phantom A (2mm, 15% salt), phantom B (4mm, 15% salt) and phantom C (6mm, 15% salt) are listed below for comparison with $\varepsilon=0.3$.

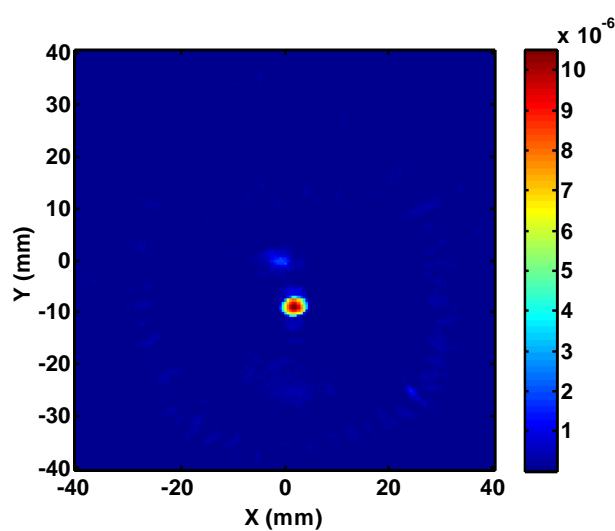


Figure 4-25. Imaging Result with 2mm phantom using RCB

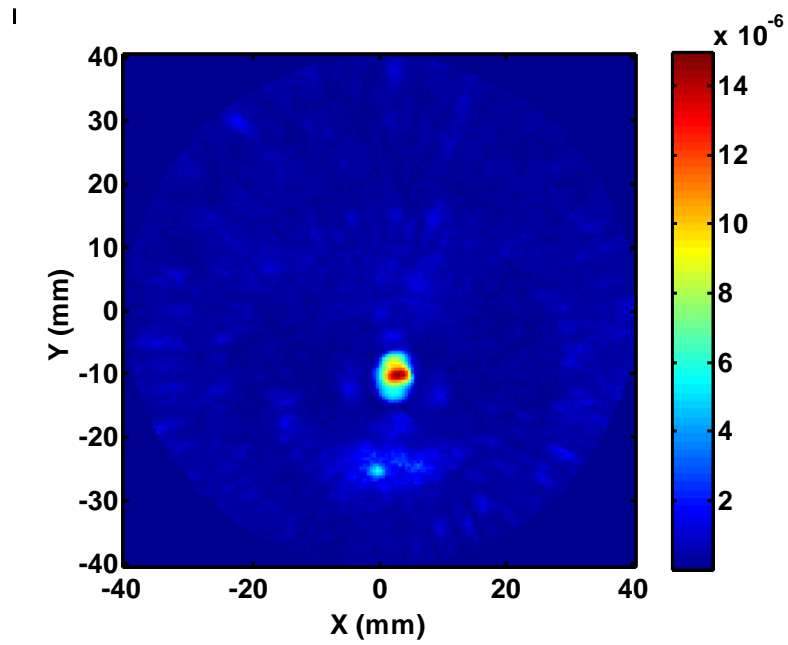


Figure 4-26. Imaging Result with 4mm phantom using RCB

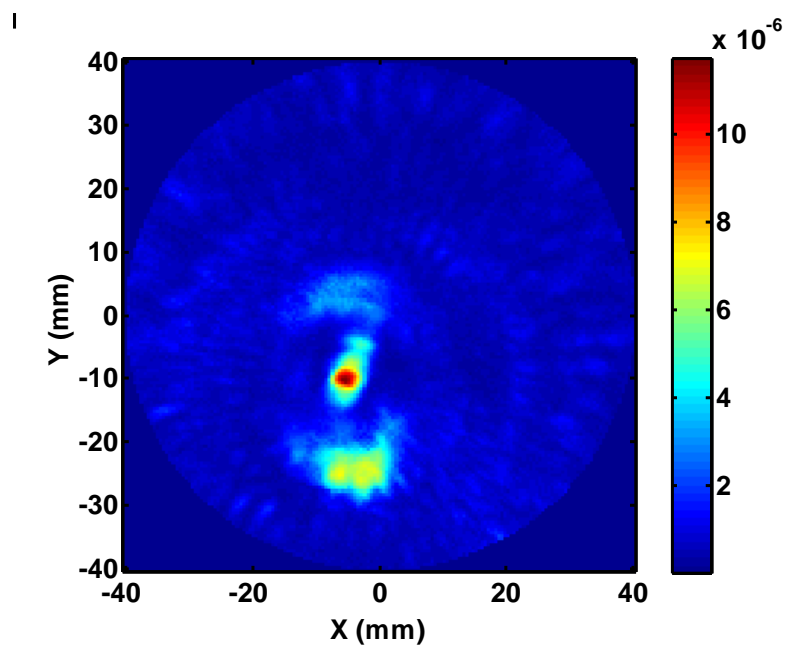


Figure 4-27. Imaging Result with 6mm phantom using RCB

Regarding spatial resolution, many factors could come into play. The bandwidth of transducer can affect pulse width of thermoacoustic signal, which can blur the image boundary and reduce spatial resolution. Large pulse width of microwave stimulation also

reduces spatial resolution. Alignment errors between phantom and transducer array could hurt the consistency of images for phantom during different experimental runs. For rough estimates, we could get an approximate spatial resolution based on the simple reasoning below. Assume that pulse width of thermoacoustic pressure wave under delta heating is Δ_{thermo} , pulse width of microwave stimulation is Δ_{mw} and the frequency bandwidth of transducer is Δ_f MHz. Roughly speaking, pulse width of the impulse response for transducer is $\Delta_{tran} = 1/\Delta_f$. According to convolution equation (2-21) and (2-22), pulse width of the piezoelectric signal received by transducer could be estimated as below:

$$\Delta_{piezo-electric} = \Delta_{thermo} + \Delta_{mw} + \Delta_{tran} \quad (4-1)$$

and then spatial resolution could be estimated as:

$$\Delta_{res} = \Delta_{piezo-electric} \cdot c_s \quad (4-2)$$

where c_s is speed of sound. If we substitute microwave pulse width 0.75 us and transducer frequency bandwidth 0.65 MHz into equations above, we could end up with the spatial resolution at least 3.4 mm.

CHAPTER 5 CONCLUSION

5.1 Contribution

In this thesis, a theoretical and experimental study of thermoacoustic imaging system is presented, together with some research findings in hardware implementation of imaging algorithm, namely Robust Capon Beamforming algorithm. The initial imaging results are obtained based on experimental data and dedicated imaging algorithm, which show the proof-of-principle study. Further research of the imaging results is restricted by limitations of current experimental setup.

Theoretical analysis about thermoacoustic signal generation by CW microwave stimulation is presented, including AM modulation technique and Diebold analysis [30] for thermoacoustic signal generation. After theoretical analysis, experimental results are presented with no observable thermoacoustic signal recorded. In reasoning for the absence of thermoacoustic signal, it is pointed out that peak power of CW microwave is too low to generate any observable signal compared with successful thermoacoustic signal generation under pulsed microwave stimulation. In CW stimulation, heat conduction might hurt the resonance of phantom through damping effects. RF safety concern also limits the highest CW RF power which can be used in medical application. As a result, we switched to pulsed microwave stimulation.

Two FPGA implementations for narrow-band and wideband RCB are performed in Xilinx Virtex4 SF35 platform device [52][53], which is specialized in signal processing application. Current implementation can successfully fit an 8 channel wideband RCB beamformer into the chip, while actual working algorithm used to get initial imaging results is based on a 24 channel RCB beamformer. In order to entirely put current

imaging algorithm in real-time implementation, a larger FPGA device should be selected for implementation or some modifications should be done to reduce the hardware utilization rate with penalty of longer latency.

The series of experiments for thermoacoustic imaging under pulsed microwave stimulation has been performed, including initial signal generation experiments and later imaging experiments. The preliminary images are obtained to serve as a successful proof-of-principle study. Several major limitations of current experimental platform are listed as follow. First, alignment between experimental tank (therefore phantom) and transducer array subsystem is an issue, which can affect the imaging result in various aspects. Second, the bandwidth of transducer could be increased, and microwave pulse width could be reduced to achieve higher spatial resolution according to equation (4-1). Non-uniform distribution of electromagnetic field inside experiment tank can be partially improved by some techniques, such as waveguide array power feeding, although it is expensive.

5.2 Future Work

In previous section, major accomplishments and limitations of our thermoacoustic imaging research have been summarized. Generally speaking, theoretical analysis, experimental investigation and practical implementation of imaging algorithm are involved. Based on limitations of current system, future works are laid out as follow. New acoustic sensor or MEMS sensor array with wider frequency response and smaller size will be deployed for signal reception. Shorter microwave pulse will be used, together with newer acoustic sensor, to improve spatial resolution of the image. New microwave power system might be designed to improve the homogeneity of electromagnetic field distribution, which could reduce imaging artifacts. More aggressive

hardware implementation of RCB algorithm could be investigated to boost computation for image reconstruction.

LIST OF REFERENCES

- [1] G. Ku and L. V. Wang, "Scanning thermoacoustic tomography in biological tissue," *Med. Phys.*, vol. 27, no. 5, pp. 1195-1202, May. 2000.
- [2] M. Pramanik, G. Ku, C. Li and L. V. Wang, "Design and evaluation of a novel breast cancer detection system combining both thermoacoustic (TA) and photoacoustic (PA) tomography," *Med. Phys.*, vol. 35, no. 6, pp. 2218-2223, Jun. 2008.
- [3] R. A. Kruger, K. K. Kopecky and A. M. Aisen, etc, "Thermoacoustic CT with Radio Waves: A Medical Imaging Paradigm," *Radiology*, vol. 121, no. 1, pp. 275-278, Apr 1999.
- [4] B. Guo, "Microwave Techniques for Breast Cancer Detection and Treatment," *PhD Thesis*, University of Florida, Gainesville, FL, 2007.
- [5] G. Ku, B. D. Fornage and L. V. Wang, etc, "Thermoacoustic and Photoacoustic Tomography of Thick Biological Tissues toward Breast Imaging," *Technology in Cancer Research & Treatment*, vol. 4, no. 5, pp. 559-565, Oct 2005.
- [6] T. Bowen, "Radiation Induced Thermoacoustic Soft Tissue Imaging," *Ultrasonics Symposium*, pp. 817-822, 1981.
- [7] J. C. Lin and K. H. Chan, "Microwave Thermoelastic Tissue Imaging : System Design," *IEEE Transactions on Microwave Theory and Techniques*, vol. 32, no. 8, pp. 854-860, Aug 1984.
- [8] L. V. Wang, X. Zhao, H. Sun and G. Ku, "Microwave-induced acoustic imaging of biological tissues," *Review Of Scientific Instruments*, vol. 70, no. 9, pp. 3744-3748, Sep 1999.
- [9] G. Ku and L. V. Wang, "Scanning microwave-induced thermoacoustic tomography: Signal, resolution, and contrast," *Med. Phys.*, vol. 28, no. 1, pp. 4-10, Jan 2001.
- [10] Y. Xu and L. V. Wang, "Signal processing in scanning thermoacoustic tomography in biological tissues," *Med. Phys.*, vol. 28, no. 7, pp. 1519-1524, Jul 2001.
- [11] D. Feng, Y. Xu, G. Ku and L. V. Wang, "Microwave-induced thermoacoustic tomography: Reconstruction by synthetic aperture," *Med. Phys.*, vol. 28, no. 12, pp. 2427-2431, Dec 2001.
- [12] M. Xu, G. Ku and L. V. Wang, "Microwave-induced thermoacoustic tomography using multi-sector scanning," *Med. Phys.*, vol. 28, no. 9, pp. 1958-1963, Sep 2001.

- [13] M. Xu and L. V. Wang, "Time Domain Reconstruction for Thermoacoustic Tomography in a Spherical Geometry," *IEEE Trans. Medical Imaging*, vol. 21, no. 7, pp. 814-822, Jul 2002.
- [14] M. Xu and L. V. Wang, "Pulsed-microwave-induced thermoacoustic tomography: Filtered backprojection in a circular measurement configuration," *Med. Phys.*, vol. 29, no. 8, pp. 1661-1669, Aug 2002.
- [15] Y. Xu, D. Feng and L. V. Wang, "Exact Frequency Domain Reconstruction for Thermoacoustic Tomography I: Planar Geometry," *IEEE Trans. Medical Imaging*, vol. 21, no. 7, pp. 823-828, Jul 2002.
- [16] Y. Xu, M. Xu and L. V. Wang, "Exact Frequency Domain Reconstruction for Thermoacoustic Tomography II: Cylindrical Geometry," *IEEE Trans. Medical Imaging*, vol. 21, no. 7, pp. 829-833, Jul 2002.
- [17] M. Xu, Y. Xu and L. V. Wang, "Time Domain Reconstruction Algorithms and Numerical Simulations for Thermoacoustic Tomography in Various Geometries," *IEEE Trans. Biomedical Engineering*, vol. 50, no. 9, pp. 1086-1099, Sep 2003.
- [18] Y. Xie, B. Guo, J. Li and L. V. Wang, etc, "Adaptive and Robust Methods of Reconstruction for Thermoacoustic Tomography," *IEEE Trans. Biomedical Engineering*, vol. 55, no. 12, pp. 2741-2752, Dec 2008.
- [19] M. Pramanik, G. Ku and L. V. Wang, etc, "Design and Evaluation of a Novel Breast Cancer Detection System Combining Both Thermoacoustic and Photoacoustic Tomography," *Med. Phys.*, vol. 35, no. 6, pp. 2218-2223, Jun 2008.
- [20] R. A. Kruger, D. R. Reinecke and G. A. Kruger, "Thermoacoustic computed tomography – technical considerations," *Med. Phys.*, vol. 26, no. 9, pp. 1832-1837, Sep 1999.
- [21] R. A. Kruger, W. L. Kiser, K. D. Miller and H. E. Reynolds, "Thermoacoustic CT: Imaging Principles," *Proc. SPIE.*, vol. 3916, no. 150, Jan 2000.
- [22] R. A. Kruger and W. L. Kiser, "Thermoacoustic CT of the Breast: Pilot Study Observations," *Proc. SPIE.*, vol. 4256, Jan 2001.
- [23] R. A. Kruger, K. Stantz and W. L. Kiser, "Thermoacoustic CT of the Breast," *Medical Imaging 2002: Physics of Medical Imaging*, pp. 521-525, May 2002.
- [24] R. A. Kruger, W. L. Kiser and K. D. Miller, etc, "Thermoacoustic CT Scanner for Breast Imaging: Design Considerations," *Proc. SPIE.*, vol. 3982, pp. 354-359, 2000.
- [25] R. A. Kruger, R. B. Lam and D. R. Reinecke, etc, "Co-registered Photoacoustic, Thermoacoustic and Ultrasound Mouse Imaging," *Proc. SPIE.*, vol. 7564, 2010.

- [26] L. Zeng, D. Xing and H. Gu, etc, "A Fast Microwave-induced Thermoacoustic Tomography System for Imaging of Biological Tissues," *Proc. SPIE.*, vol. 6047, 2006.
- [27] L. Nie, D. Xing and D. Yang, etc, "Microwave-induced Thermoacoustic Imaging Enhanced with a Microwave Contrast Agent," *IEEE/ICME International Conference on Complex Medical Engineering*, pp. 989-993, 2007.
- [28] C. Cao, L. Nie and D. Xing, etc, "The Feasibility of Using Microwave-induced Thermoacoustic Tomography for Detection and Evaluation of Renal Calculi," *Physics in Medicine and Biology*, vol. 55, pp. 5203-5212, 2010.
- [29] J. Li, P. Stoica and Z. Wang, "On Robust Capon Beamforming and Diagonal Loading," *IEEE Trans. Signal Processing*, vol. 51, no. 7, pp. 1702-1715, Jul 2003.
- [30] G. J. Diebold and P. J. Westervelt, "The Photoacoustic Effect Generated by a Spherical Droplet in a Fluid," *Journal of the Acoustical Society of America*, vol. 84, no. 6, pp. 2245-2251, Dec 1988.
- [31] *IEEE Standard for Safety Levels with Respect to Human Exposure to Radio Frequency Electromagnetic Fields, 3 kHz to 300 GHz*, pp. 6-15, 1999.
- [32] J. Litva and K. Y. Lo Titus, "Digital Beamforming in Wireless Communications," *Artech House Publishers*, 1996.
- [33] J. Li and P. Stoica, "Robust Adaptive Beamforming," *Wiley*, 2006.
- [34] B. D. Van Veen and K. M. Buckley, "Beamforming: A Versatile Approach to Spatial Filtering," *IEEE ASSP Magazine*, pp. 4-24, 1988.
- [35] C. Dick and F. Harris, "Real-Time QRD-Based Beamforming on an FPGA Platform," *IEEE Fortieth Asilomar Conference on Signals, Systems and Computers*, 2006.
- [36] F. Edman, "Digital Hardware Aspects of Multiantenna Algorithms," *PhD Thesis*, Lund University, 2006.
- [37] A. Irturk, S. Mirzaei and R. Kastner, "FPGA Implementation of Adaptive Weight Calculation Core Using QRD-RLS Algorithm," *UCSD Technical Report*, CS2009-0937D.
- [38] H. Wang, M. Mohr and M. Glesner, "Hardware Implementation of Adaptive Beamformers Used for Smart Antennas," *EuCAP*, Nov 2007.
- [39] J. Gotze, S. Paul and M. Sauer, "An Efficient Jacobi-like Algorithm for Parallel Eigenvalue Computation," *IEEE Transactions on Computers*, Sep 1993.

- [40] R. Andraka, "A Survey of CORDIC Algorithms for FPGA Based Computers," *Proceeding of ACM/SIGDA Sixth International Symposium on Field Programmable Gate Arrays*, pp. 192-200, Feb 1998.
- [41] J. Liu, B. Weaver and Y. Zakharov, "An FPGA-Based MVDR Beamformer Using Dichotomous Coordinate Descent Iterations," *IEEE International Conference on Communications*, 2007.
- [42] G. E. Forsythe and P. Henrici, "The Cyclic Jacobi Method For Computing the Principal Values of A Complex Matrix," *Transactions of the American Mathematical Society*, Jan 1960.
- [43] N. D. Hemkumar, "Efficient VLSI Architectures for Matrix Factorizations," *PhD Thesis*, Rice University, Apr 1994.
- [44] K. Minseok, K. Ichige and H. Arai, "Design of Jacobi EVD Processor Based On CORDIC for DOA Estimation With MUSIC Algorithm," *The 13th IEEE International Symposium on PIMRC 2002*, vol. 1, pp. 120-124, Sep 2002.
- [45] Radio-Research Instrument Co, *Operational Manual of 70 kW RF Package*, 2010.
- [46] Olympus Panametrics NDT, *Transducer Test Report*, Mar 2005.
- [47] Olympus Panametrics NDT, *Model 5800: Ultrasonic Pulser/Receiver User's Manual*, 2005.
- [48] National Instruments, *NI PXI-5122 High Resolution Digitizer Datasheet*.
- [49] R. L. Nasoni, G. A. Evanoff and P. G. Halverson, "Thermoacoustic Emission by Deeply Penetrating Microwave Radiation," *Ultrasonic Symposium*, pp. 633-638, 1984
- [50] R. A. Kruger, "Thermoacoustic Computed Tomography Scanner," *US Patent File 6216025*, Apr 2001.
- [51] K. M. Reddy and T. J. Herron, "Computing the Eigen Decomposition of a Symmetric Matrix in Fixed-point Arithmetic", *Tenth Annual Symposium on Multimedia Communications and Signal Processing*, Nov 23, 2001.
- [52] X. Guan, H. Zmuda, etc, "Hardware Implementation of Wideband Time-domain Robust Capon Beamforming", *2011 IEEE International Symposium on Antennas and Propagation*, pp. 2849 – 2852, Jul 2011
- [53] X. Guan, H. Zmuda, etc, "FPGA Implementation of Robust Capon Beamforming", *SPIE 2012 Medical Imaging Conference*, Feb 2011

BIOGRAPHICAL SKETCH

Xin Guan was born in Baoji City, Shaan Xi province, P. R. China on 1982. Xin Guan received Bachelor of Science in Tsinghua University, Beijing, P. R. China, majoring in Engineering Physics. After that, Xin Guan got Master of Science in Tsinghua Accelerator Lab in Department of Engineering Physics. During that time, Xin Guan studied and researched on the S-band photo-injector for microwave linear accelerator. After the master's studies, Xin Guan came to University of Florida, Gainesville, FL for PhD in the Electrical and Computer Engineering Department. During his PhD studies, Xin Guan was primarily involved in the experimental research on the Thermoacoustic Imaging System. Xin Guan's research interests lie in the medical imaging, microwave engineering, digital signal processing and hardware implementation of DSP algorithm.